Nano Research Energy

ISSN 2791-0091 (print); 2790-8119 (online)
https://doi.org/10.26599/NRE.2025.9120214

Review Article

Metal organic frameworks-derived hollow functional materials: Synthetic strategies and electrocatalytic applications

Qingqing Yang[1,2,§], Hao Wan[1,2,3,4,§], Ying Zhang[1,2,3,4,§], Songtao Zhang[5], Xiaohe Liu[1,2,3,4], Renzhi Ma[6], and Hairong Xue[1,2,3,4] (✉)

[1] *Zhongyuan Critical Metals Laboratory, Zhengzhou University, Zhengzhou 450001, China*
[2] *School of Chemical Engineering, Zhengzhou University, Zhengzhou 450001, China*
[3] *Zhongyuan Critical Metals Laboratory, Zhengzhou 450001, China*
[4] *State Key Laboratory of Critical Metals Beneficiation, Metallurgy and Purification, Zhengzhou 450001, China*
[5] *Testing Center, Yangzhou University, Yangzhou 225009, China*
[6] *Research Center for Materials Nanoarchitectonics, National Institute for Materials Science (NIMS), Namiki 1-1, Tsukuba, Ibaraki 305-0044, Japan*
[§] *Qingqing Yang, Hao Wan, and Ying Zhang contributed equally to this work.*

Received: 13 October 2025 / **Revised:** 21 November 2025 / **Accepted:** 3 December 2025 / **Published date:** 8 January 2026

ABSTRACT

Hollow nanostructure materials derived from metal-organic frameworks (MOFs) have many promising applications in electrochemical energy storage and conversion, benefiting from their large specific surface area and void space, accelerating electron and mass transport. Significant efforts have been devoted to designing and fabricating hollow materials with manipulated geometric morphology, optimized electronic structure, and diverse composition. This review summarizes the current research progress of MOF-derived hollow materials for electrocatalysis. Here, we commence with the synthesis strategies for MOF-derived hollow functional materials, providing a comprehensive overview of design approaches for hollow structures. These encompass acid etching, ion exchange, templating methods, and autocatalytic pyrolysis, demonstrating the rich possibilities and advantages in designing and synthesising MOF-derived hollow materials. Subsequently, we focus on representative advances in the application of MOF-derived hollow materials within the field of small-molecule conversion, including hydrogen evolution reactions, oxygen evolution reactions, and oxygen reduction reactions. Finally, synthesis optimization and application prospects of MOF-derived hollow materials are provided.

KEYWORDS

metal-organic framework, hollow structure, nanomaterials, controllable synthesis, electrochemical applications

1 Introduction

The increasing global consumption of conventional fossil fuels, escalating energy demands, and worsening environmental issues have propelled rapid advancements in renewable energy technologies [1]. Central to this transition is the growing need for advanced energy conversion/storage devices, including fuel cells [2–5], water electrolyzers [6–8], and rechargeable batteries [9–11]. However, the performance of electrode materials, as critical components in these devices, remains suboptimal. To date, significant efforts have been devoted to designing and developing cost-effective, durable electrode materials with enhanced functionality [12–15].

Metal-organic frameworks (MOFs) have emerged as a rapidly expanding research frontier due to their structural designability, diverse building units, and tunable architectures [16, 17]. Benefiting from uniform pore structures, adjustable porosity, atomic-level uniformity, and vast compositional diversity, MOFs have been extensively explored for energy conversion and storage applications since their discovery [18–22]. Compared to pristine MOFs, their derivatives inherit porous characteristics while exhibiting superior stability, electrical conductivity, and electrochemical properties, making them highly attractive for electrocatalysis [23–25]. Electrocatalytic reactions are inherently complex processes involving multiple steps and intermediates [26, 27]. The activity and selectivity of these reactions are predominantly governed by the adsorption/desorption energetics of intermediates on catalyst surfaces [28–30], with charge state modulations significantly influencing intermediate binding dynamics [29, 31]. Consequently, both the density of active sites and their intrinsic activity are critical determinants of electrocatalytic performance [32–34]. Rational engineering of geometric configurations and electronic structures offers a

Address correspondence to Hairong Xue, xuehairong@zzu.edu.cn

promising approach to achieve electrocatalysts with exceptional activity and selectivity.

The physical and chemical properties of materials are jointly determined by their structural and compositional characteristics. In the case of MOFs, their synthesis dictates their unique porous architectures and tunable chemical compositions. MOFs exhibit distinct advantages as precursors for constructing functional materials. Their morphologies are well-preserved during thermal transformation processes, wherein controlled growth of MOF precursors enables the fabrication of diverse carbon-based materials, including one-dimensional (1D) nanorods, two-dimensional (2D) nanobelts, and three-dimensional (3D) hierarchical porous architectures [35, 36]. Furthermore, the unique benefits of MOF precursors are fully manifested in the synthesis of hollow structures. These hollow architectures, characterized by high surface areas and open frameworks, provide abundant active edges and exposed catalytic sites, thereby enhancing their electrochemical performance [37–41].

In this review, we systematically summarize synthesis strategies for MOF-derived hollow structures, with a focus on acid etching, ion exchange, templating approaches, and self-catalytic pyrolysis (Fig. 1). We subsequently discuss their applications as advanced electrode materials in key electrocatalytic processes, including the oxygen evolution reaction (OER), hydrogen evolution reaction (HER), and oxygen reduction reaction (ORR). Finally, we present critical perspectives on existing challenges and future directions for the rational design of MOF-derived hollow architectures.

2 Synthesis methods for MOF-derived hollow structures

2.1 Synthesis strategies for MOF-derived hollow structures

The properties of materials are determined by their internal microstructure. While different types of materials inherently possess distinct properties, even the same material can exhibit varying properties when subjected to different processing techniques that result in distinct microstructures. The distinctive configuration of hollow materials confers a multitude of advantageous properties, including enhanced surface-to-volume ratio, diminished density, micro-reactor environments, higher loading capacity, and diminished mass and charge transport lengths. Consequently, hollow materials have garnered significant attention for future technological applications. The fabrication of hollow structural materials remains a prominent research domain. Initial methodologies were confined to controlled synthesis and regulation at macro- and micro-scales via methods such as spray drying and purging [42]. In 1998, Caruso pioneered the synthesis of hollow silica and silica-polymer hybrid spheres using micelles as templates [43], thereby establishing templating as a universal paradigm for hollow material synthesis. In recent years, a variety of synthetic strategies for hollow structural materials have been investigated, with concise overviews of the formation mechanisms of each approach (Fig. 2). These processes primarily include template-mediated assembly, stepwise dissolution-re-growth via Oswald ripening, and selective chemical etching. Notwithstanding substantial accomplishments, the controlled synthesis of porous/hollow materials with meticulously engineered structures (particularly complex ones) and precise compositions continues to pose significant challenges.

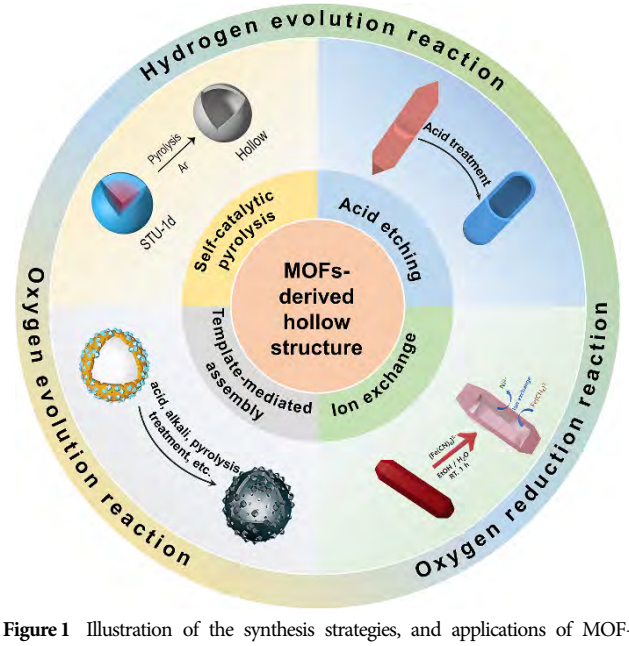

Figure 1 Illustration of the synthesis strategies, and applications of MOF-derived hollow structures.

MOFs represent a class of materials formed by the coordination of organic ligands with metal ions or metal clusters through coordination bonds. The resulting materials show many advantages, such as open lattice structure, high porosity, structural flexibility, and tunability [44, 45]. However, MOFs also show some inherent limitations. Their chemical stability is relatively poor, and their electrical conductivity is limited. These constraints restrict their application in electrocatalysis as well as energy conversion and storage [46]. The inherent structural characteristics of MOFs make them ideal precursors or templates for obtaining derivatives with different morphologies or compositions by composition modification or transformation control during thermal treatment [47]. Three main morphological control strategies for MOFs have been identified: (i) Control of the crystallization process or incorporation of templates to inherit the morphological features of MOF precursors; (ii) Introduction of reducing gases into the system during thermal decomposition or placement of components that can generate reducing gases upstream, as well as control of morphological changes by gas release from MOFs during thermal decomposition [48]; (iii) Rigorous treatments, such as chemical modification and thermal activation, on carbon materials obtained after thermal decomposition [49]. The unique advantages of MOFs as precursors are fully demonstrated in the synthesis of hollow materials. Due to their distinctive porous structures and tunable chemical compositions, MOFs enable the controlled preparation of hollow nanostructures. In recent years, efforts have been dedicated to the development of multiple innovative synthesis methodologies for constructing hollow MOFs with heterostructures [50]. Notably, both solid-liquid reactions and thermal treatments are often employed in tandem. The solid-liquid reaction method is a widely used technique for constructing hollow structures, including etching, ion exchange, and template-assisted methods.

2.2 Acid etching

The acid etching technique is recognized as an important synthetic strategy for fabricating hollow-structured materials, capitalizing on the inherent differential chemical stability between internal and exterior domains within MOFs crystals [51]. The

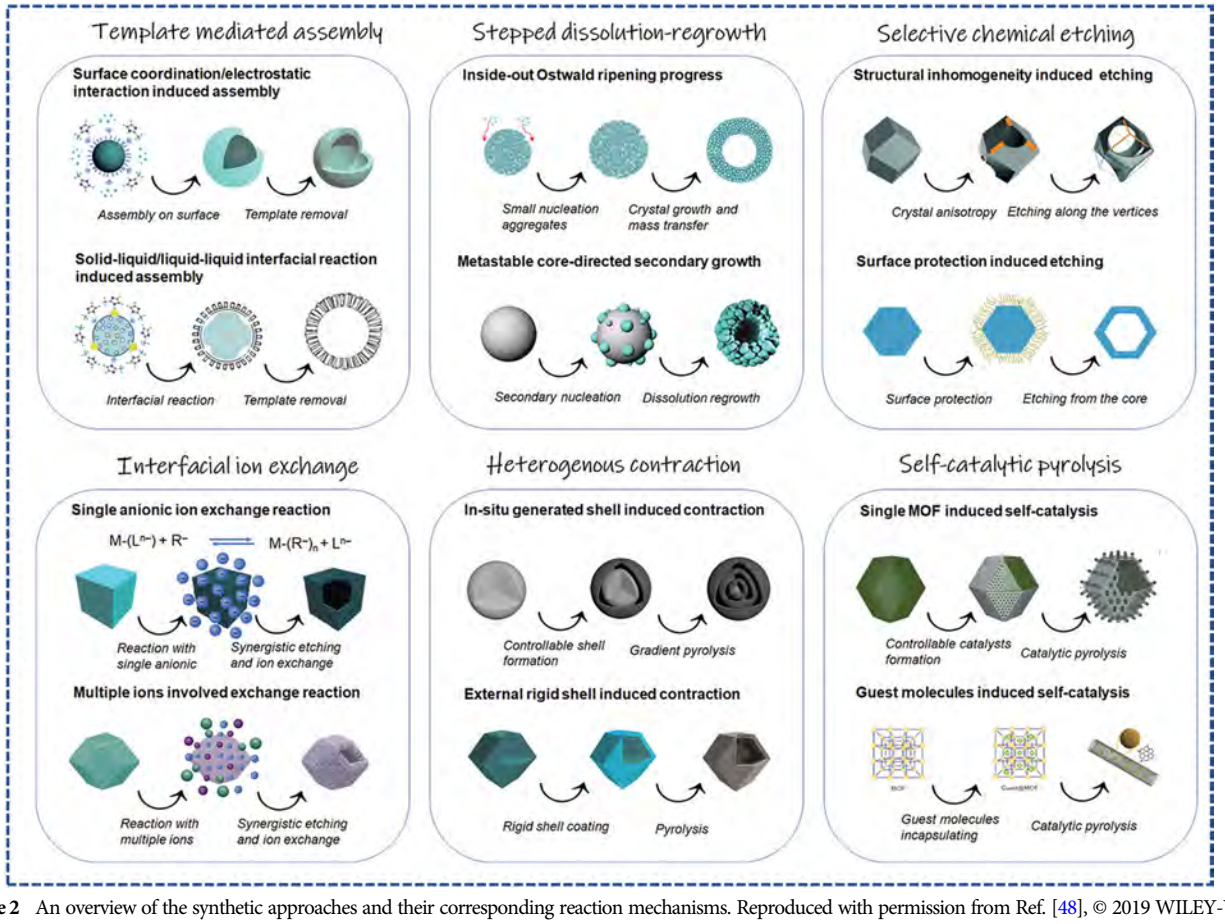

Figure 2 An overview of the synthetic approaches and their corresponding reaction mechanisms. Reproduced with permission from Ref. [48], © 2019 WILEY-VCH Verlag GmbH & Co. KGaA, Weinheim.

structural heterogeneity of MOFs crystals originates from anisotropic distributions of metal-ligand bond densities and defect populations along distinct crystallographic orientations during crystal growth [52]. This structural non-uniformity, coupled with the labile nature of metal-ligand coordination bonds, enables the acid-induced structural decomposition of MOFs crystals through accelerated hydrolysis of coordination bonds in acidic media [53]. The derivatives of MOFs into hollow metal organic frameworks (HMOFs) with high surface areas and active sites show promising potential for enhancing the rates of ORR, HER, and OER. Moreover, non-precious metal-based catalysts exhibit excellent activity and stability, making them ideal candidates for improving catalytic performances for ORR, HER, and OER [46].

Phosphate-based ligands, such as phytic acid ($C_6H_6(H_2PO_4)_6$), possess strong chelating abilities, which can act as both a phosphorus source and an etching agent. Their interaction with MOFs can produce hollow transition metal phosphide. For example, our group had reported a novel hollow leaf-like Co_2P/N-doped porous carbon (Co_2P-NC) composite, synthesized using polydopamine (PDA)-coated Co-doped zeolitic imidazolate framework nanoleaf (Co-ZIF-L) as precursors and phytic acid (PA) as both an etching agent and phosphorus source (Figs. 3(a)–3(c)) [54]. The hollow architecture was formed through a one-step pyrolysis process (Fig. 3(d)), driven by etching and coordination reactions between PA and the leaf-like Co-ZIF-L. In the as-prepared transition metal phosphide (TMPs)/carbon composite, Co_2P nanoparticles are encapsulated and uniformly dispersed within the 2D hollow leaf-like N-doped porous carbon matrix. Owing to its structural and compositional advantages, the Co_2P-NC catalyst exhibits remarkable catalytic activity and durability for both the HER and OER, as well as overall water splitting (OWS) in alkaline media. The authors emphasize that, compared to conventional gas–solid reaction methods for TMPs synthesis, this strategy offers a safer and more straightforward approach, demonstrating significant feasibility for designing hollow TMPs/porous carbon composites. Similarly, Li et al. employed ZIF-67 as a precursor to fabricate hollow dodecahedral structures through phytic acid treatment, which was further pyrolyzed to obtain hollow HCoP/C composite (Fig. 3(e)) [55]. The dodecahedral ZIF-67 (as shown in Fig. 3(f)) was first synthesized, followed by the gradual addition of a mixed phytic acid/ethanol solution ($V_{\text{phytic acid}}$: V_{ethanol} = 1:40) into an ethanol solution containing ZIF-67 and polyvinylpyrrolidone (PVP) (Fig. 3(g)). This process effectively preserved the morphology of material while inducing hollow structure, as illustrated in Fig. 3(h). During thermal treatment, the cleavage of P-O bonds in the phosphate groups of phytic acid released phosphorus ions, which reacted with Co ions to form CoP. In the etching process, protons released by phytic acid diffused into the ZIF-67 core, gradually forming a core-shell structure. The surface-functionalized PVP effectively inhibited the penetration of phytic acid ions into the ZIF-67 framework, thus preventing structural collapse of the ZIF-67 dodecahedrons. In addition, Lou et al. utilized MIL-88A as a precursor through phytic acid treatment, demonstrating high activity and exceptional stability for water electrolysis across a full pH range (Fig. 3(i)) [56]. The Fe-based MIL-88A hexagonal nanorods were first synthesized and the effect of Ni doping on their morphology was subsequently investigated. With increasing

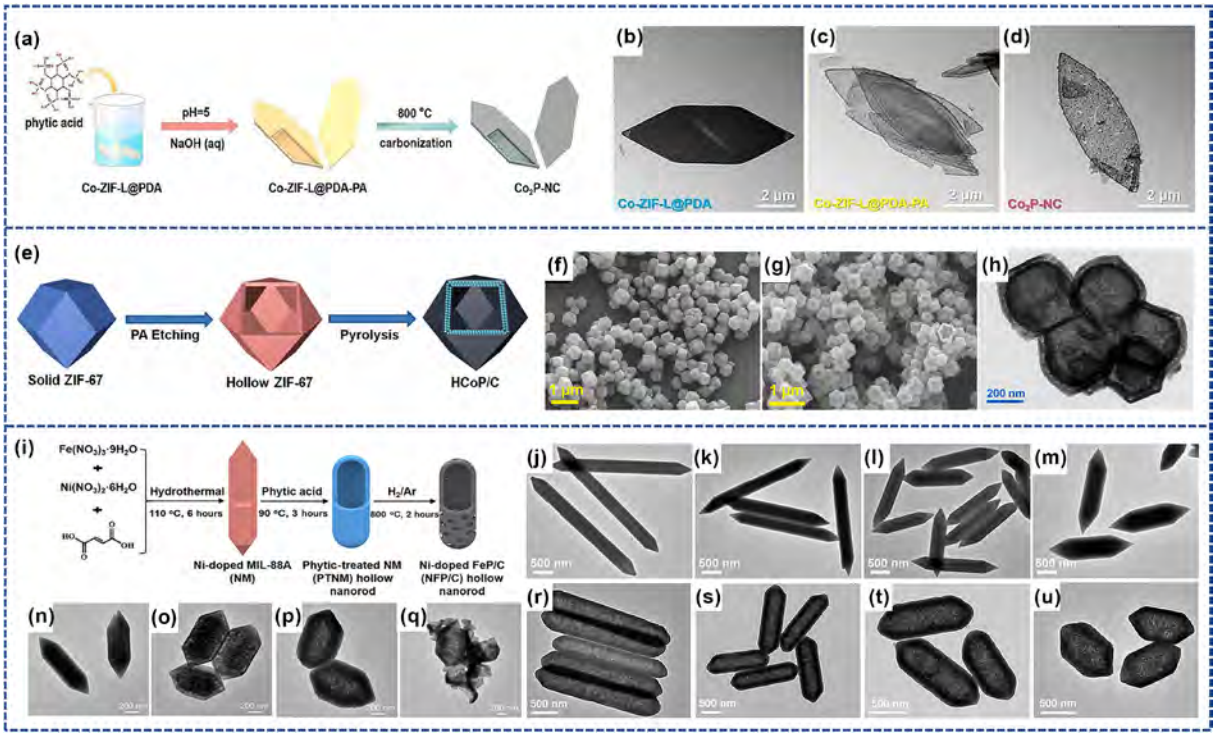

Figure 3 (a) Schematic illustration of the preparation of Co_2P-NC composite. (b)–(d) Transmission electron microscopy (TEM) images of Co-ZIF-L@PDA, Co-ZIF-L@PDA-PA and Co_2P-NC samples. (a–d) Reproduced with permission from Ref. [54], © 2024 Published by Elsevier B.V. (e) Schematic illustration of the HCoP/C catalyst fabrication process. (f) Scanning electron microscopy (SEM) image of pristine ZIF-67 crystals, (g) SEM and (h) TEM images of acid-etched ZIF-67 derivatives. (e–h) Reproduced with permission from Ref. [55], © 2024 Elsevier Ltd. (i) Synthetic schematic of Ni-doped FeP/C hollow nanorods. TEM images depict: (j) pristine MIL-88A and (r) its phosphoric acid-treated counterpart (90 °C); (k–m) Ni-doped MIL-88A nanorods with Ni/Fe atomic ratios of 1:3, 2:2, and 3:1, respectively, alongside their phosphoric acid-treated derivatives (s-u, 90 °C); (n–q) temperature-dependent morphological evolution (30 °C, 60 °C, 90 °C, 120 °C) of Ni-doped MIL-88A under phosphoric acid treatment. (i–u) Reproduced with permission from Ref. [56], © 2019 Lu, X. F. et al.

Ni doping contents, the average length of the material decreased from 3.2 to 1.6 μm, while the average width increased from 400 to 600 nm, as shown in Figs. 3(j)–3(m). Furthermore, the influence of etching temperature (30 °C, 60 °C, 90 °C, and 120 °C) on the morphology was explored. As the temperature increased, the nanorods gradually transformed into well-dispersed hollow particles with core-shell/yolk-shell structures or aggregates of small hollow nanoparticles, as illustrated in Figs. 3(n)–3(q). After treatment with 0.1 M PA at 90 °C, both MIL-88A and Ni-doped MIL-88A samples underwent coordination and etching processes, where the solid inner layers were etched away to form hollow rod-like nanostructures. While the overall morphology was preserved, the aspect ratio of the nanorods changed, as depicted in Figs. 3(r)–3(u).

Tannic acid (TA) is also commonly used as etching agents, not only increasing the number of surface activity sites but also protecting metal ions and enhancing the performance of catalysts [57]. Additionally, TA possesses a large number of phenolic hydroxyl groups, which can significantly improve the stability of MOFs [58]. As exemplified by Lv et al., ZIF-67 nanocube precursor was subjected to etching with tannic acid, resulting in the formation of ZIF-67 nanoboxes structure, as shown in Fig. 4(a) [59]. More specifically, ZIF-67 nanocubes were prepared by using tetradecyltriamethylbromochalkoform (CTAB) as a capping agent. Due to etching and coordination of tannic acid, ZIF-67 hollow nanoboxes were obtained, as illustrated in Figs. 4(c) and 4(d). Subsequently, ion exchange between ZIF-67 hollow nanoboxes and 2,3,6,7,10,11-hexaiminotriphenylene (HTP) ligands was employed to assemble Co-MOF nanoboxes, as shown in Figs. 4(e) and 4(f). The strong chelating ability of the HTP ligand caused the aggregation of numerous Co-MOF nanoparticles into well-organized nanobox structures, facilitating the exposure of active sites and enhancing liquid mass transfer, thus significantly improving the electrocatalytic performance [60, 61]. Moreover, density functional theory (DFT) calculations revealed that the Co-N_4 center in a low-spin state with atom dispersion acts as the catalytic active site [59]. Li et al. developed a unique etching functionalization strategy to construct single-flavonoid functionalized MOFs with a distinctive combination of hollow walls and 3D ordered macroporous (H-3DOM) structures, as illustrated in Figs. 4(g)–4(k) [62] . These MOFs, using single-flavonoids as precursors, were further used to synthesize Co-loaded carbon materials with H-3DOM structures and a hydrophilic surface by high-temperature pyrolysis. Single-flavonoids, characterized by their rich oxygen-containing functional groups and appropriate acidity, serve as effective etching agents. They not only selectively etch the inner walls of the macro pores to create hollow structures but also introduce abundant oxygen-containing functional groups on the sample surface, thereby forming a hydrophilic surface and enhancing liquid mass transfer efficiency. Utilizing tetradecylthiosulfate (TAA) to etch MOF precursors provides a direct route to hollow metal sulfide materials.

It has been demonstrated that using TAA as an etchant is an effective method for creating central pores and depositing metal sulfides [63–65]. Yang et al. utilized a cobalt-based metal-organic framework (Co-MOF) as both a precursor and a self-sacrificial template, successfully synthesizing highly hierarchical MoS_2/CoS_2 nanotube arrays through TAA-based selective etching (Fig. 5(a)) [66]. The process begins with the growth of 1D Co-MOF

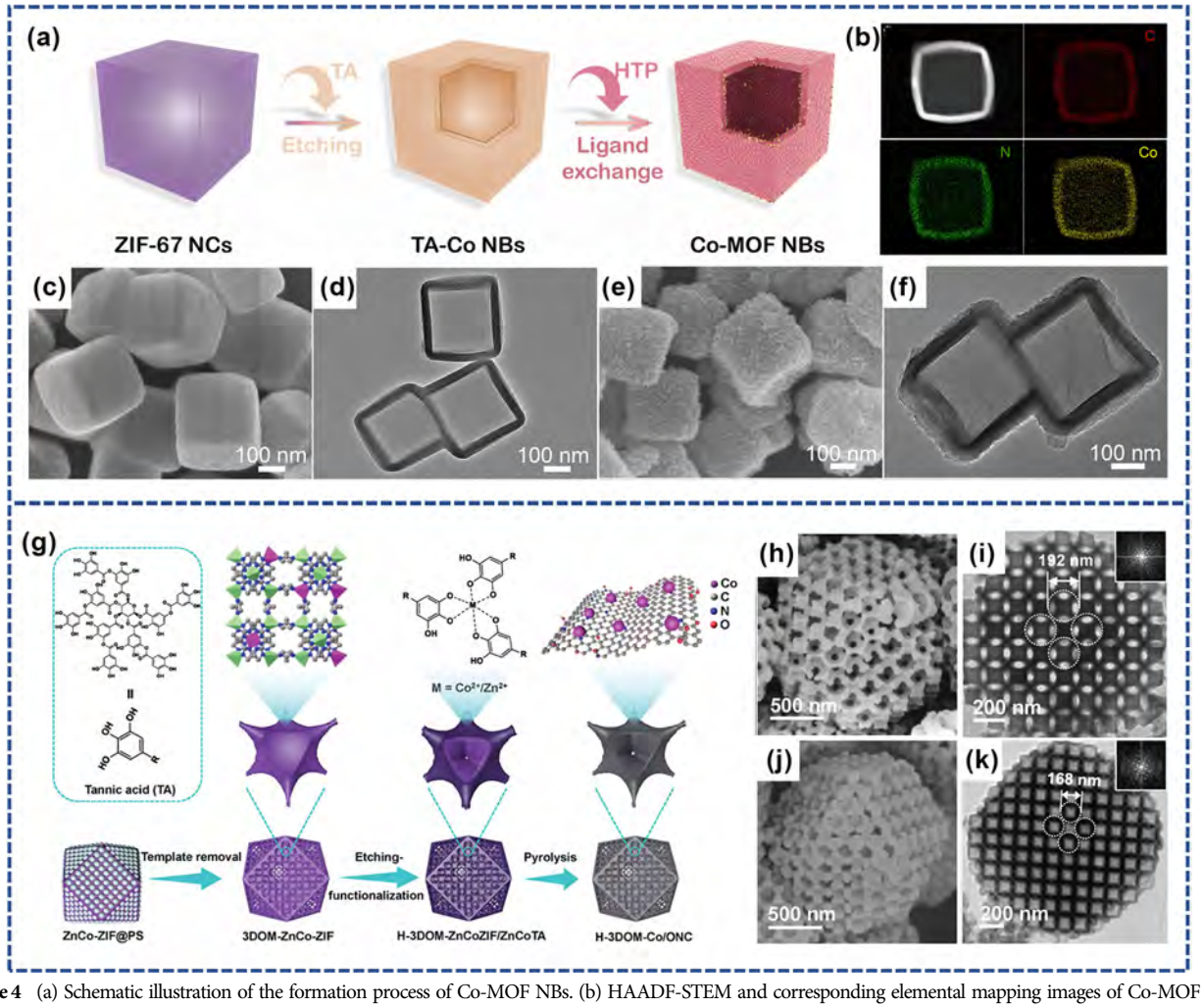

Figure 4 (a) Schematic illustration of the formation process of Co-MOF NBs. (b) HAADF-STEM and corresponding elemental mapping images of Co-MOF NBs; (c) SEM and (d) TEM images of TA-Co NBs. (e) SEM and (f) TEM images of Co-MOF NBs. (a–f) Reproduced with permission from Ref. [59], © 2024 Elsevier B.V. (g) Fabrication process of hierarchically porous 3D-ordered macroporous Co/N-doped carbon (H-3DOM-Co/ONC). (h) SEM and (i) TEM images of 3DOM-ZnCo-ZIF precursor. (j) SEM and (k) TEM images of H-3DOM-ZnCoZIF/ZnCo TA hybrid. (g–k) Reproduced with permission from Ref. [62], © 2023 Wiley-VCH GmbH.

nanotube arrays on carbon paper using 2-merimidium and cobalt nitrate hexahydrate ($Co(NO_3)_2{\cdot}6H_2O$). Subsequently, the simple hydrothermal reactions were employed to deposit ultra-thin 2D MoS_2 nanosheets on the Co-MOF surfaces in an ammonium tetramolybdate ($(NH_4)_2MoS_4$) solution. Co-MOF can provide abundant surface anchoring sites for the MoS_2 nucleation occurred on the Co-MOF surface. Simultaneously, Co^{3+} ions derived from the Co-MOF can serve as *in-situ* catalysts, which lead to the transformation of Co-MOF into CoS_2 on the carbon paper, forming MoS_2/CoS_2 solid nanowires. Finally, selective etching with TAA solutions was performed on the MoS_2/CoS_2 solid nanowires, resulting in nanotube arrays assembled with MoS_2 nanosheets with hollow structure, as depicted in Figs. 5(b)–5(g). Generally, TAA hydrolyzes to produce hydrogen sulfide and acid, which act as dual etching agents. The produced acid not only induces Co^{3+} ions to transform into Co^{2+} ions, forming CoS_2 on the carbon paper but also promotes the in suit deposition of CoS_2 via reaction with hydrogen sulfide. The hierarchical MoS_2/CoS_2 nanotube arrays exhibit good HER performance across the full pH range. DFT calculations reveal that the strong interface interactions at the heterogeneity interface play a pivotal role in enhancing HER performance by increasing the electronic states at S-S edges. This increase in electronic states lowers the Gibbs free energy of H_2 adsorption and reduces the activation energy barrier for water splitting, thereby improving the overall catalytic efficiency of the nanotube arrays. Similarly, Zhang et al. employed TAA as both an etching agent and sulfur source to synthesize MOF-derived hollow Zn-Co-Ni sulfide (ZCNS) nano-sword arrays, with the experimental workflow illustrated in Fig. 5(h) [67]. Initially, 1D ZnCo MOF solid nano-sword arrays were grown on nickel foam (NF) via a hydrothermal reaction. Subsequently, a secondary hydrothermal treatment using TAA as the dual-functional etchant/sulfur precursor yielded the ZCNS nano-sword arrays, as depicted in Figs. 5(i)–5(n). Notably, TAA simultaneously etched the NF substrate to generate nickel sulfide phases. Throughout the sulfidation-etching process, progressive S^{2-} substitution within the organic framework of ZnCo MOF facilitated the formation of hollow ZCNS architectures. The resultant hollow ZCNS nano-sword arrays exhibited exceptional electrocatalytic activity and stability for both the HER and OER. The coexistence of (i) $Co_9S_8(111)@Ni_3S_2(101)$ heterointerfaces and (ii) ZnS(111) crystallographic facets within the ZCNS matrix promotedlocalized charge redistribution, thereby enhancing interfacial charge transfer kinetics. DFT calculations revealed that the heterostructure synergistically modulates the electronic states of Co_9S_8 and Ni_3S_2, significantly lowering the energy barriers for rate-determining steps in both HER and OER pathways.

In previous reports, triply bonded thiouracil acid (TTCA) has

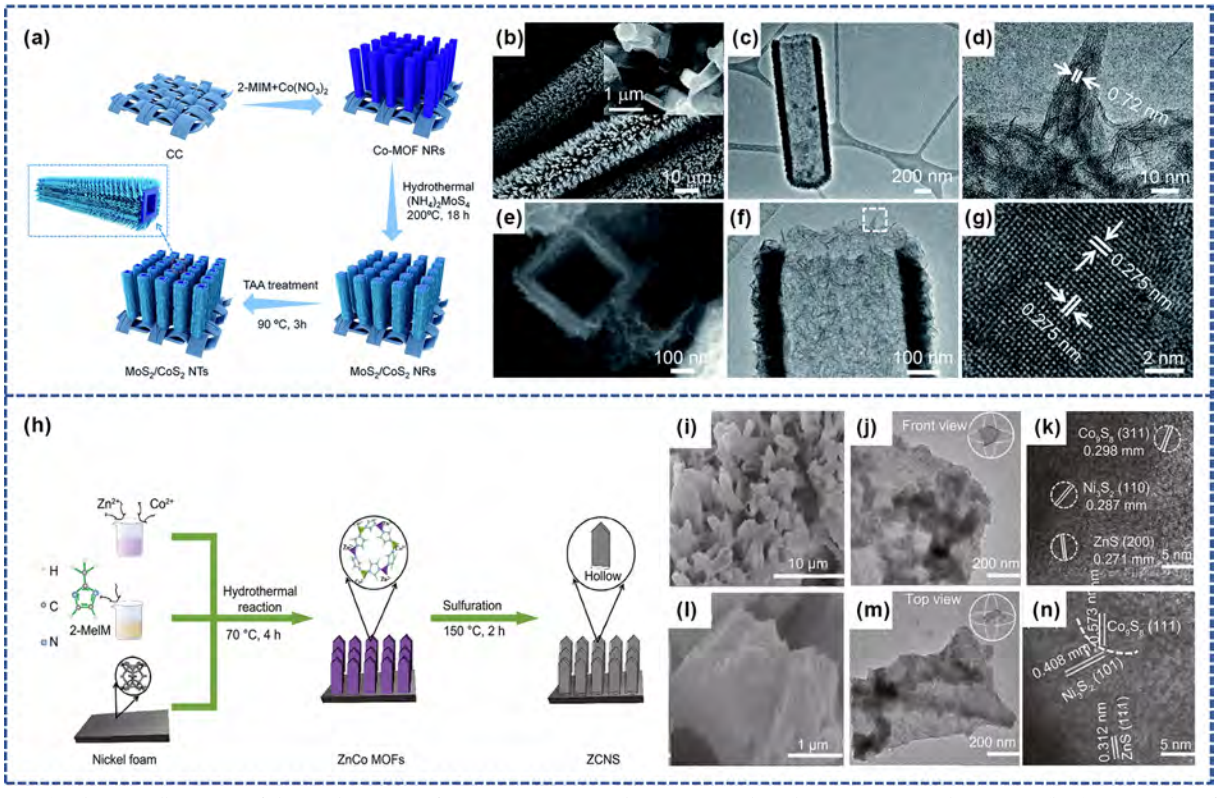

Figure 5 (a) Schematic illustration of the synthesis route for 2D/1D MoS_2/CoS_2 heterostructured catalysts grown on carbon paper. (b, e) SEM and (c, f) low-magnification TEM images of MoS_2/CoS_2 NTs. (d) Enlarged TEM view of the marked region in (f), revealing vertically aligned MoS_2 nanosheets with layered morphology. (g) High-resolution TEM (HRTEM) image confirming the coexistence of crystalline CoS_2 phases. (a–g) Reproduced with permission from Ref. [66], © 2019 The Royal Society of Chemistry. (h) Synthesis pathway for MOF-derived hollow Zn-Co-Ni sulfide (ZCNS) nanosword arrays (NSAs). (i, l) SEM images at varying magnifications, and (j, k) cross-sectional versus (m, n) top-view TEM images of individual ZCNS units. (h–n) Reproduced with permission from Ref. [67], © 2021 Institute of Process Engineering, Chinese Academy of Sciences.

been widely used as both a sulfur source and a carbon source to synthesize cobalt-based catalysts such as Co_9S_8 [68]. However, its application as an etchant and its potential for forming porous structures directly through interaction with MOFs has not been reported. For the first time, Wang et al. successfully synthesized nitrogen and sulfur-doped porous CoP carbon nanocages by employing TTCA not only as an etchant but also as a sulfur source [69]. TTCA exhibits strong chelating abilities with metal ions, enabling direct interaction with the MOF framework. During the etching process, Co ions bind to TTCA and form Co-KY complexes on the ZIF-67 surface, resulting in a shell structure. As the etching proceeds inwardly, metal ions migrate outward while S ions migrate inward, leading to differences in their diffusion rates. This causes progressive shell breakdown within the ZIF-67 framework, ultimately forming a porous shell structure. By adjusting the etching time and calcination temperature, optimal HER performance under alkaline conditions can be achieved. The mechanism reveals that sulfur doping and calcination significantly enhance HER activity. This improvement is attributed to the synergistic effects between the metal elements Co and non-metal elements S, which collectively enhance the catalytic performance, while also exhibiting excellent cyclic stability.

Through etching strategies, not only heteroatoms such as P and S can be introduced, but also single metal atoms. For instance, Huang et al. employed a selenic acid etching-assisted approach to obtain isolated metal-semimetal diatomic catalysts (DACs) [70]. First, the ZIF-8 precursor was etched with SeO_2, followed by calcination. During calcination, evaporated Se species were reduced and doped into the nitrogen-doped carbon (NC) substrate, forming an atomically dispersed Se catalyst (Se-NC) with a hierarchical hollow nanostructure. Subsequently, Fe atoms were adsorbed and anchored onto the Se-NC framework, yielding highly dispersed Fe-Se DAC materials via thermal activation. Mechanism studies indicate that the synergistic effect of Fe-N_4 and Se-C_2 atomic configurations endows Fe-Se DAC with outstanding CO_2 reduction reaction (CO_2RR) activity. Concurrently, the electronic configuration at Fe-Se hybrid sites promotes CO_2 activation and optimises the binding strength of key intermediates at active sites, thereby enhancing CO_2 conversion rates.

The acid etching strategy remains a prevalent methodology for synthesizing hollow-structured materials. Contemporary implementations predominantly employ organic acids characterized by high molecular weights and inherent structural configurations that confer strong chelating capacity toward metal ions. During etching processes, these macromolecular acids form protective layers on MOF surfaces through coordinate bonding, effectively mitigating over-etching phenomena. Besides, beyond their primary etching function, such organic acids concomitantly introduce heteroatoms (e.g., P, S and Se) into the material matrix, thereby streamlining synthesis protocols through multifunctional reagent utilization. However, current research on acid etching mechanisms remains insufficiently explored, with particularly limited investigations into etching condition optimization. Systematic studies are urgently required to establish a comprehensive theoretical framework governing etching thermodynamics/kinetics and structure-property correlations. Moreover, introducing gas-releasing substances during pyrolysis can also achieve acid etching effects, enabling

relatively straightforward synthesis of hollow functional materials. For instance, Zhu et al. employed a gas diffusion strategy to synthesise bowl-shaped porous nano-Pb single-atom catalysts (Pb SAC) featuring a highly asymmetric coordination microenvironment [71].

2.3 Ion exchange strategy

The solid-state MOFs precursor reacts with suitable chemical agents in solution to form a rigid shell at the solid-liquid interface, while simultaneously transforming or etching the core to create hollow structures. This strategy has been widely employed for converting solid MOFs into hollow multifunctional materials. The formation of hollow architectures can be achieved via anion-exchange reactions between anionic ligands in MOFs precursors and solution-phase reactants, which drive the chemical transformation of MOFs into structurally engineered hollow configurations.

For example, Kim et al. synthesized NiFe-PBA hollow nanorods (NiFe-PBA HNRs) using a Ni-based MOF as both precursor and self-sacrificing template through an ion-exchange strategy (Fig. 6(a)) [72]. The authors first synthesized Ni-MOF nanorods via ultrasonic synthesis and used them as self-sacrificial templates to homogeneously mix them with $K_3[Fe(CN)_6]$ solution for ion exchange reaction. The Ni^{2+} cations from the Ni-MOF interior diffused outward to react with the $[Fe(CN)_6]^{3-}$ anion, and in the process, the internal Ni-MOF was completely converted into PBA, resulting in hollow architecture, as depicted in Figs. 6(b) and 6(c). Finally, a distinctive hollow carbon material incorporating Ni-Fe mixed metal phosphides and amorphous carbon was successfully synthesized via high-temperature calcination and phosphidation under an argon atmosphere, as illustrated in Figs. 6(d) and 6(e). Notably, the shell composed of numerous Ni_2P and Fe_2P nanoparticles displayed porous characteristics, exposing more active sites and facilitating electrolyte diffusion. Metal species incorporated through ion-exchange processes not only generate monometallic nanoparticles but also form alloy phases with host metal species within MOFs, demonstrating a versatile synthetic strategy for hybrid nanocomposites. Zhang et al. reported the synthesis of CoRu alloy/N-doped carbon hollow nanomaterials (CoRu@NCHNs) (Fig. 6(f)) [73]. Using ZIF-67 as precursor, they introduced Ru^{3+} cations through ion exchange while simultaneously incorporating nitrogen atoms via dopamine (DA) addition. The strong coordination between DA and Co ions induced ZIF-67 structural decomposition, releasing alkaline 2-methylimidazole. Under alkaline conditions, DA underwent self-polymerization to form PDA shells encapsulating ZIF-67, while Ru^{3+} was simultaneously incorporated into the PDA shell through strong synergistic interactions, resulting in CoRu/PDA HNS hollow nanostructures, as shown in Figs. 6(g)-6(i) [74]. Subsequent pyrolysis produced CoRu@NCHNs with well-preserved morphology. It's noteworthy that the CoRu/PDA HNS exhibited rough surfaces due to fine PDA particulates. During pyrolysis, organic ligands underwent reductive decomposition at elevated temperatures, reducing metal ions to metallic species and nanoparticles, thereby enhancing material conductivity.

The traditional hollow frameworks show well-defined internal spaces and large surface areas, which have been extensively studied. However, these frameworks exhibit high transmission resistance and limited accessibility of internal space owing to their rigid structure. Following this approach, Shi et al. utilized the *in-situ* self-sacrificial template strategy of MOFs, synthesize Co/CoO heterojunction (Co/CoO@HNC) fixed on spinel-like hollow nitride-doped carbon (the synthesis process illustrated in Fig. 6(j) [75]. By employing MIL-88A as the self-sacrificial template (Figs. 6(k) and 6(o)), pyrole and $(NH_4)_2S_2O_8$ were introduced into the system. The positively charged pyrole was attracted and adsorbed onto the negatively charged MIL-88A surface, while $(NH_4)_2S_2O_8$ served as the initiator to promote poly-pyrole formation. During the polymerization of pyrole, the free H^+ ions

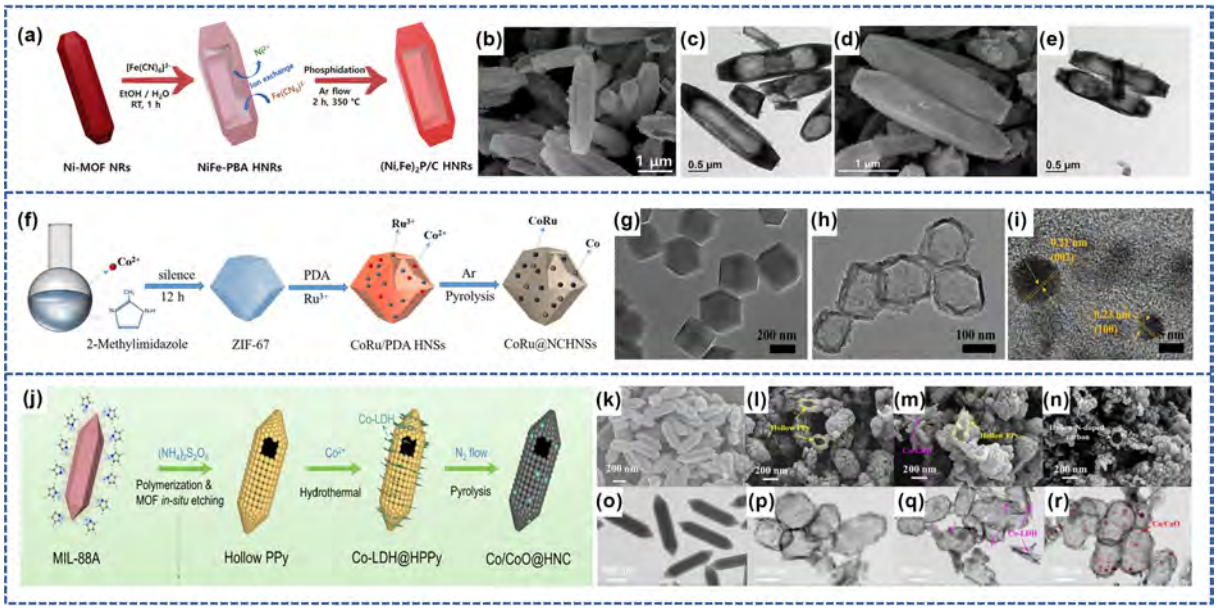

Figure 6 (a) Schematic illustration of the synthesis of (Ni, Fe)$_2$P/C hollow nanorods (HNRs). (b) SEM and (c) TEM images of NiFe-PBA HNRs; (d) SEM and (e) TEM images of (Ni, Fe)$_2$P/C HNRs. (a-e) Reproduced with permission from Ref. [72], © 2022 The Royal Society of Chemistry. (f) Schematic illustration of the synthesis of CoRu@NCHNSs. (g) and (h) TEM images of ZIF-67 and CoRu/PDA hollow nanospheres (HNSs), and (i) HR-TEM image of CoRu/PDA HNSs. (f-i) Reproduced with permission from Ref. [73], © 2024 The Royal Society of Chemistry. (j) Schematic illustration of the synthesis process of Co/CoO@HNC. (k) SEM and (o) TEM images of MIL-88A; (l) SEM and (p) TEM images of HPPy nanocages; (m) SEM and (q) TEM images of Co-LDH@HPPy; (n) SEM and (r) TEM images of Co/CoO@HNC. (j-r) Reproduced with permission from Ref. [75], © 2022 Elsevier B.V.

facilitated the coordination of the organic ligand, leading to the cleavage of Fe-O bonds in MIL-88A through ion exchange. This process resulted in the complete dissolution of MIL-88A (Figs. 6(l) and 6(p)). Subsequently, under simple hydrothermal conditions, Co^{2+} underwent hydrolysis to generate a cobalt-based layered double hydroxide (Co-LDH) on the hollow poly-pyrole nanocage framework, as illustrated in Figs. 6(m) and 6(q). Finally, the Co-LDH underwent thermal decomposition to yield Co/CoO@HNC in an N_2 atmosphere at 700 °C. The external framework of Co/CoO@HNC is assembled from interconnected nitrogen-doped carbon spheres (Figs. 6(n) and 6(r)), effectively preserving the orthogonal spinel-like hollow structure of Co-LDH@HPPy, as shown in Fig. 6(q). The incorporation of Co/CoO@HNC significantly modifies the local electronic environment, enhancing the electron transfer capability and improving the catalytic performances of oxygen reduction and oxidation reactions.

In addition, Wang et al. developed binder-free $NiCo_2O_4$ hollow nano-wall arrays through a sequential ion-exchange/etching strategy (Fig. 7(a)) [76]. The synthesis was initiated with the epitaxial growth of 2D cobalt-metal organic framework (2D Co-MOF) nanosheet arrays on conductive carbon cloth via a coordination-driven precipitation process (Figs. 7(b) and 7(c)). A subsequent anion-exchange-etching treatment using $Ni(NO_3)_2$ solution induced structural evolution from dense MOF walls to porous $NiCo_2O_4$ hollow configurations, as depicted in Figs. 7(d)–7(g). Mechanistic analysis reveals that the hydrolysis of Ni^{2+} cations ($Ni^{2+} + H_2O \rightarrow Ni(OH)^+ + H^+$) generates acidic microenvironments that simultaneously: (1) etch the organic framework through proton-assisted ligand dissolution, and (2) drive the interfacial co-precipitation of Ni-Co layered double hydroxide (LDH) precursors. This dual-function mechanism preserves the nano-wall morphology while creating hierarchical porosity spanning meso-/macropores. The interconnected hollow architecture facilitates rapid electrolyte diffusion and exposes abundant electroactive sites, synergistically enhancing OER kinetics. Significantly, the monolithic electrode design eliminates polymeric binders, minimizing interfacial charge transfer resistance. Complementing this work, Luo et al. proposed a controlled ion exchange method to construct amorphous Zn/Co-Fe hollow nano-walls on carbon cloth (Figs. 7(h) and 7(i)) [77]. Their methodology involved first synthesizing crystalline bimetallic Zn/Co-MOF nanoarrays through controlled coprecipitation,

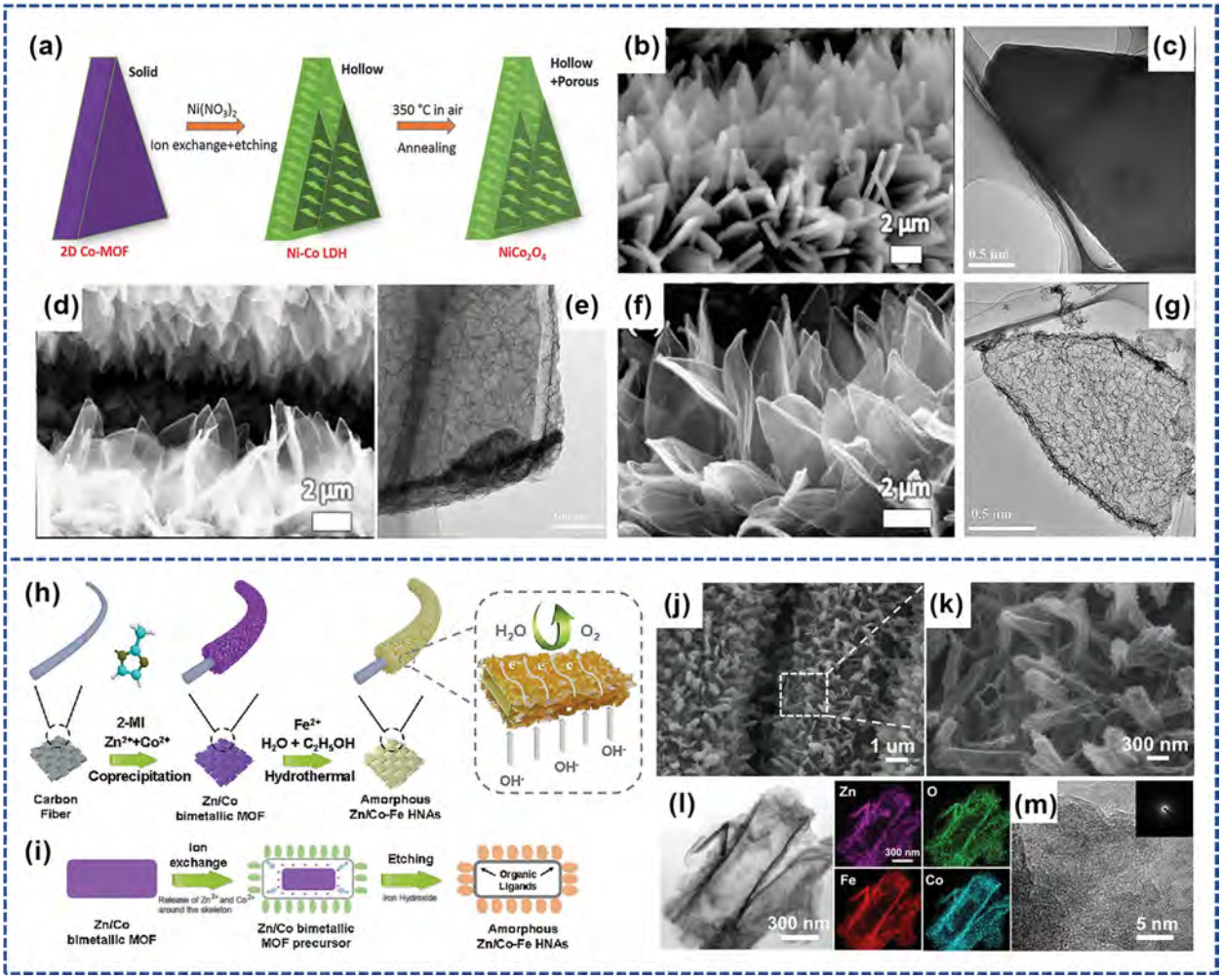

Figure 7 (a) Schematic illustration of the formation of hollow nickel-cobalt oxide nanostructures from 2D Co-MOF solid nanowalls. (b) SEM and (c) TEM images of 2D Co-MOF nanowalls; (d) SEM and (e) TEM images of Ni–Co LDH hollow nanostructures; (f) SEM and (g) TEM images of $NiCo_2O_4$ hollow nanostructures. (a–g) Reproduced with permission from Ref. [76], © 2017 WILEY-VCH Verlag GmbH & Co. KGaA, Weinheim. (h) Synthesis process for bimetallic-MOF-derived amorphous Zn/Co–Fe HNAs on carbon cloth. (i) Schematic illustration of the construction of bimetallic-MOF-derived amorphous Zn/Co–Fe HNAs by an ion-exchange and etching strategy. (j) and (k) SEM images of bimetallic Zn/Co MOF-derived amorphous Zn/Co–Fe HNAs at different magnifications; (l) and (m) TEM and HRTEM images of a single Zn/Co bimetallic amorphous MOF-derived Zn/Co–Fe hollow nanowalls and its element mapping of Zn, Co, Fe, O as well as the selected area electron diffraction pattern in the inset. (h–m) Reproduced with permission from Ref. [77], © 2021 Wiley-VCH GmbH.

followed by Fe^{2+}-mediated structural reconstruction. During the ion-exchange phase, Fe^{2+} hydrolysis ($Fe^{2+} + 2H_2O \rightarrow Fe(OH)_2 + 2H^+$) induces proton-driven ligand dissociation, disrupting the original Zn/Co-MOF coordination network. The released Zn^{2+} and Co^{2+} ions subsequently react with ferric hydroxide to form amorphous Zn/Co-Fe hollow nano-wall arrays, as depicted in Figs. 7(j)–7(m).

The ion-exchange strategy represents another prevalent approach for synthesizing hollow-structured materials, fundamentally operating through solid-liquid interfacial reactions. The ionic substitution pathways are governed by the chemical nature of reactant species in the liquid phase, thereby enabling controlled introduction of foreign metal ions-either singular or multiple-into the framework. This mechanism serves as a versatile platform for fabricating bimetallic or multimetallic MOFs with tailored compositional complexity.

2.4 Template-assisted methods

The template-directed approach has emerged as a fundamental strategy for fabricating porous materials through controlled sacrificial templating mechanisms. This methodology enables precise construction of porous architectures via a sequential fabrication process: initially forming core-shell composite precursors through surface templating, followed by structural consolidation and subsequent template elimination while preserving morphological integrity. The paramount advantage of this technique stems from the inherent replicability of template geometries, allowing systematic regulation of pore dimensions and material morphology through judicious template selection and optimized coating parameters. Current template classification systems typically differentiate three principal categories based on template characteristics and interaction mechanisms: self-templating processes, hard-template replication, and soft-template approaches.

2.4.1 *Self-template method*

Recent advancements have demonstrated that hollow MOF nanostructures can be engineered through dissolution-regrowth mechanisms, with Ostwald ripening and metastable core-directed secondary growth processes emerging as prominent pathways [78]. These template-free strategies streamline synthetic workflows by eliminating the need for exogenous templates, thereby enhancing process efficiency and reducing manufacturing costs.

Ostwald ripening has been established as an efficient self-templating strategy for fabricating hollow architectures, with widespread applications in nanomaterial synthesis. This thermodynamically driven process involves the dissolution of smaller crystals/colloidal particles and subsequent redeposition of dissolved species onto larger particles, governed by the Gibbs-Thomson principle [79]. Due to their higher surface energy, smaller crystallites undergo preferential dissolution and recrystallization, as their elevated Gibbs free energy significantly enhances solubility compared to larger counterparts. The formation of hollow structures via this mechanism arises from the inward-to-outward diffusion of dissolved species from smaller internal aggregates to larger external crystals. A representative demonstration by Kim et al. utilized Ostwald ripening to synthesize Se-doped CoS_2 hollow nanospheres (Fig. 8(a)) [80]. Template-free ZIF-67 precursors were initially prepared through coordination-driven crystallization in methanol containing $CoSO_4 \cdot 7H_2O$ and 2-methylimidazole, as depicted in Fig. 8(b). Methanol's low dielectric constant (ε=32.7) reduces critical nucleus radius, elevating solution supersaturation to enable rapid homogeneous nucleation of spherical particles. The strong coordination capability of SO_4^{2-} anions facilitated extensive decomposition of Co^{2+}-2-methylimidazole complexes in ZIF-67, triggering an inside-out ripening mechanism. This process featured mass transfer from small-grained core regions to large-grained shell domains through dissolution-recrystallization

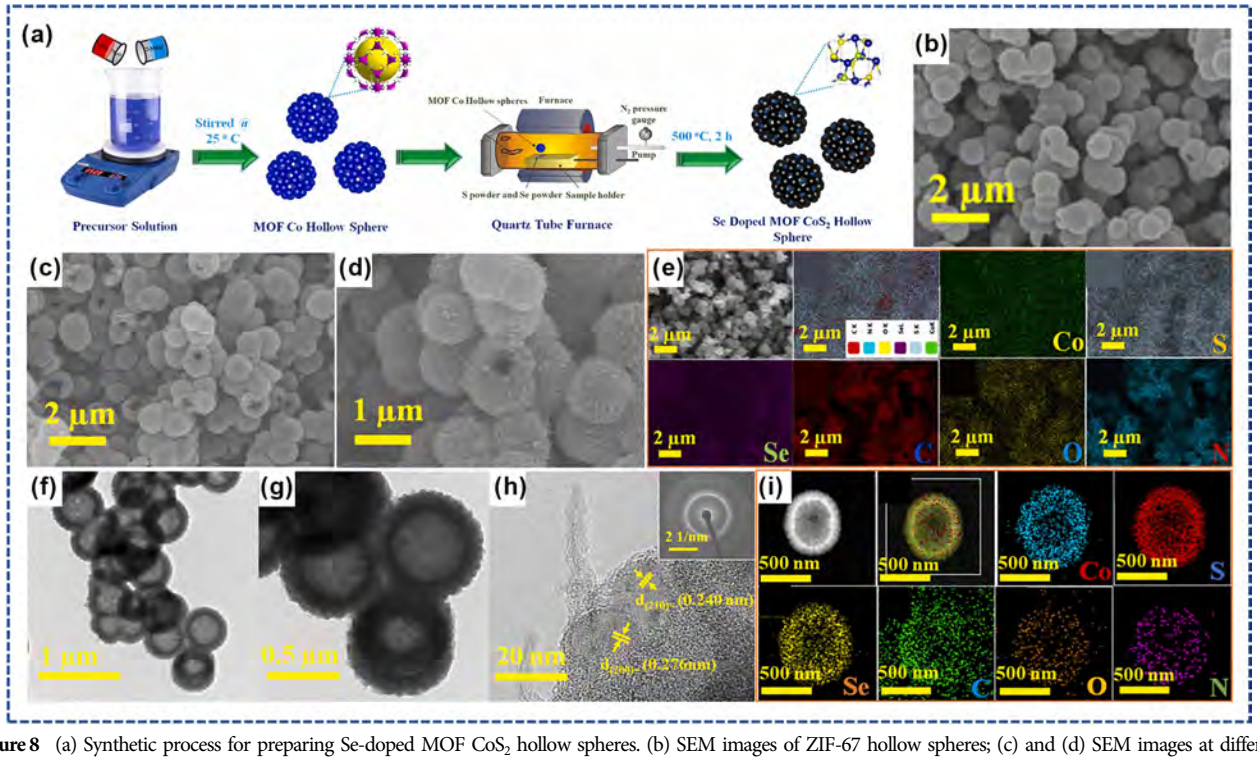

Figure 8 (a) Synthetic process for preparing Se-doped MOF CoS_2 hollow spheres. (b) SEM images of ZIF-67 hollow spheres; (c) and (d) SEM images at different magnifications, (f) and (g) TEM images, and (h) HRTEM image of Se-doped MOF CoS_2 hollow spheres at different magnifications; (e) and (i) EDX and HR-EDX mapping of Co, S, Se, C, N, and O of the Se doped MOF CoS_2 hollow spheres. (a–i) Reproduced with permission from Ref. [80], © 2023 Elsevier B.V.

kinetics. Subsequent sulfuration/selenization in a tubular furnace yielded Se-doped CoS_2 hollow spheres, as depicted in Figs. 8(c), 8(d), 8(f)–8(h). The elemental mapping demonstrated that the Co, S, Se, C, N, and O constituents are distributed uniformly throughout the product, as illustrated in Figs. 8(e) and 8(i). The product exhibited exceptional bifunctional OER/ORR catalytic activity in alkaline media. DFT calculations revealed that Se-doping optimizes the Gibbs free energy of oxygen intermediate adsorption on Co active sites, thereby enhancing intrinsic OER activity.

2.4.2 *Hard template method*

Covalently bonded rigid templates-including polymeric architectures with diverse spatial configurations, anodized aluminum oxide (AAO) membranes, porous silicon frameworks, metallic templates, natural biopolymers, zeolites, colloidal crystals, and carbon nanotubes-exhibit superior structural stability and precise nanoconfinement effects, enabling stringent control over nanoparticle dimensions and morphologies. Commonly used materials include polystyrene (PS) spheres and silica (SiO_2). This strategy primarily utilizes the coordination interaction between surface functional groups and metal nodes to coat a layer of MOF nuclei on the template surface. For example, Xue et al. prepared hollow mesoporous carbon spheres (HMCSs) and MOF-derived carbons (NC(M)/HMCSs and NC(M)@HMCSs) using SiO_2@SiO_2-PDA core-shell spheres as dual-functional templates [81], the specific synthesis process is shown in Fig. 9(a). The interfacial coating strategy involved epitaxial growth of ZIF(M) nanocrystals on SiO_2@SiO_2-PDA surfaces, followed by carbonization and template etching to yield NC(M)/HMCSs composites. In contrast, the spatial encapsulation approach first generated HMCSs via sequential pyrolysis and etching, then confined ZIF(M) growth within HMCSs cavities to construct ZIF(M)@HMCSs heterostructures. By modulating metal precursors (Mn/Co/Ni/Cu nitrates) and Zn-to-metal molar ratios, a library of HMCSs/ZIFs hybrids was synthesized, as demonstrated in Figs. 9(b)–9(k). During pyrolysis, volatile Zn species were selectively removed, while trace transition metals remained anchored on HMCSs and NC(M) matrices. The incorporation of a secondary MOF precursor as a co-precursor within the MOF-coated shell templated on a substrate enables the pyrolysis-driven formation of ultrafine alloy nanoparticles, a structural outcome unattainable through thermal decomposition of individual MOF precursors alone. For instance, Lou et al. devised a dual-MOF-assisted pyrolysis protocol to fabricate Co-Fe alloy/N-doped carbon hollow spheres using polystyrene (PS) colloidal templates (Fig. 9(l)) [82]. MIL-101 nanoparticles (50 nm), $Co(NO_3)_2{\cdot}6H_2O$, and 2-methylimidazole were sequentially introduced into PS suspensions, enabling the hierarchical assembly of MIL-101/ZIF-67 nanoshells on PS surfaces, as depicted in Fig. 9(m). Thermal

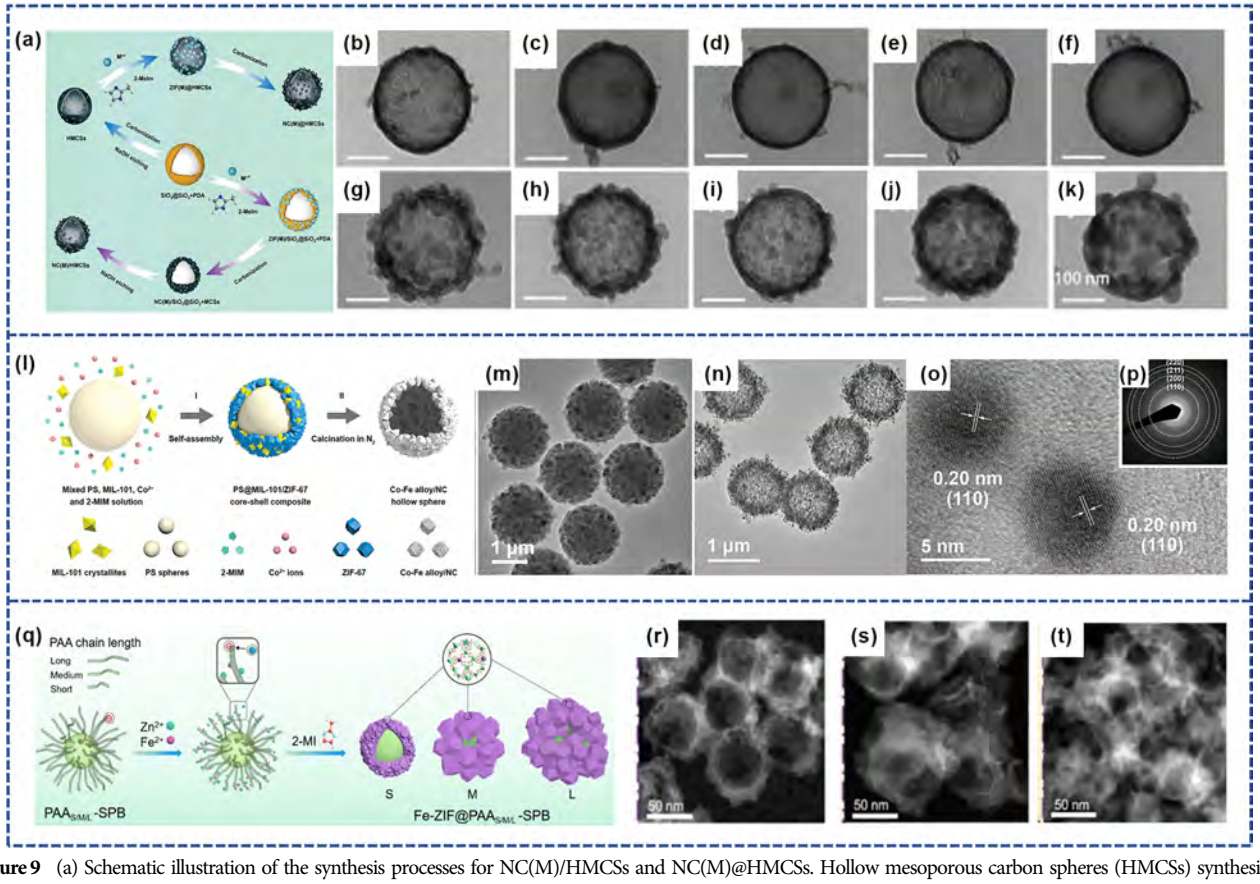

Figure 9 (a) Schematic illustration of the synthesis processes for NC(M)/HMCSs and NC(M)@HMCSs. Hollow mesoporous carbon spheres (HMCSs) synthesized via interfacial coating method: (b–f) TEM images of NC(Zn)/HMCSs, NC(Zn, Mn)/HMCSs, NC(Zn, Co)/HMCSs, NC(Zn, Ni)/HMCSs, and NC(Zn, Cu)/HMCSs, respectively. HMCSs synthesized via spatial encapsulation method: (g–k) TEM images of ZIF(Zn)@HMCSs, ZIF(Zn, Mn)@HMCSs, ZIF(Zn, Co)@HMCSs, ZIF(Zn, Ni)@HMCSs, and ZIF(Zn, Cu)@HMCSs, respectively. (a–k) Reproduced with permission from Ref. [81]. © 2024 Tang, Y. J. et al. (l) Formation process of Co-Fe alloy/N-doped carbon hollow spheres. (m) and (n) TEM images of PS@MIL-101/ZIF-67 core-shell composite and Co-Fe/NC hollow spheres, respectively. (o) and (p) HRTEM image and SAED pattern of Co-Fe/NC, respectively. (l–p) Reproduced with permission from Ref. [82], © 2019 WILEY-VCH Verlag GmbH & Co. KGaA, Weinheim. (q) Schematic illustration of the synthesis process of Fe-ZIF@PAA-SPB using templates with different PAA-SPB chain lengths. (r–t) HAADF-STEM images of s-Fe-HNC, m-Fe-HNC, and l-Fe-HNC, respectively. (q–t) Reproduced with permission from Ref. [83], © 2023 The Royal Society of Chemistry.

annealing simultaneously decomposed PS templates, obtaining hollow spheres (as shown in Figs. 9(n)–9(p)), and reduced MOF-encapsulated Fe^{3+}/Co^{2+} to homogenized Co-Fe nanoalloys. The MIL-101 co-precursor facilitated confined pyrolysis within the MOF matrix, suppressing nanoparticle coalescence. By tuning Co^{2+} concentrations and 2-methylimidazole ratios, MIL-101 loading densities in MOF shells were precisely controlled. The optimized catalyst demonstrated exceptional ORR activity and durability, attributed to synergistic effects between metallic active sites and N-doped conductive frameworks.

Beyond conventional approaches involving direct MOF core coating on template surfaces, materials derived from secondary surface-engineered templates through re-growth of MOF nuclei demonstrate substantially enhanced performance characteristics. Dai et al. developed an electrostatic confinement strategy using anionically charged spherical polyacrylic acid brushes (PAA-SPBs) as adaptive templates to synthesize ZIF-8-derived SACs with tunable hollow carbon nanostructures (Fig. 9(q)) [83]. The methodology commenced with the synthesis of monodisperse PS cores (~69 nm in diameter) via emulsion polymerization, followed by UV-initiated grafting of polyacrylic acid (PAA) chains with precisely controlled lengths onto PS surfaces. The resulting high-density anionic brush layer exhibited strong electrostatic binding capacities for cationic metal precursors (Zn^{2+}/Fe^{2+}), effectively restricting ion migration through Donnan equilibrium effects. Sequential infusion of Zn^{2+}/Fe^{2+} and 2-methylimidazole triggered confined coordination polymerization, forming Fe-doped ZIF-8 nanocrystals (Fe-ZIF@PAA-SPB) spatially constrained within the brush layer. Crucially, PAA chain length dictated final architectures. For short-chain PAA, partial protonation of -COOH groups reduced electrostatic screening, enabling internal ZIF nucleation within swollen brushes. This produced small ZIF-8 crystallites and post-pyrolysis spherical hollow N-doped carbons (s-Fe-HNC), as demonstrated in Fig. 9(r). The PAA chains induce chain collapse due to the strong adsorption of highly negatively charged carboxylate ions ($-COO^-$) toward Zn^{2+} and Fe^{2+} ions. This phenomenon concomitantly drives the formation of large-grained ZIF-8 crystallites on the PAA-SPB template surface. Consequently, the subsequent pyrolysis process yields disordered hollow architectures in both mesoporous Fe-doped hollow N-doped carbon (m-Fe-HNC) and its layered counterpart (l-Fe-HNC), as evidenced in Figs. 9(s) and 9(t). Controlled pyrolysis (900 °C, N_2) simultaneously carbonized ZIF-8 and decomposed PAA-SPB templates, retaining Fe as isolated single atoms without metallic clustering. This chain-length-dependent templating mechanism enables programmable design of SAC architectures, demonstrating structure-performance correlations in ORR.

2.4.3 *Soft template method*

Soft templates, predominantly comprising self-assembled surfactant aggregates, constitute a class of amphiphilic architectures including lyotropic liquid crystalline phases, vesicular bilayers, micellar assemblies, microemulsion droplets, Langmuir-Blodgett films, and biomimetic supramolecular frameworks. These systems leverage competing hydrophobic-hydrophilic interactions to establish spatially organized nanoreactors, enabling precise control over nucleation and crystallization dynamics.

Shahrokhian et al. developed an emulsion-directed interfacial assembly technique to architect ultrafine Ru/RuO_2 nanoclusters (<3 nm) within CuCo nitride-embedded N-doped carbon matrices (Ru/RuO_2/CuCoN@NC) (Fig. 10(a)) [84]. The hierarchical synthesis comprised three synergistic stages: (1) Aqueous nanodroplets containing Cu^{2+}/Co^{2+} and steric stabilizer PVP were homogenized in 1-octanol via high-shear emulsification. PVP's amphiphilic character generated steric-electronic stabilization, suppressing droplet coalescence. (2) Controlled infusion of 1,3,5-benzenetricarboxylate (BTC) from the organic phase induced interfacial supersaturation, driving rapid coordination polymerization at the liquid-liquid boundary. BTC's trifunctional carboxyl groups facilitated pH-modulated heterometallic coordination, yielding epitaxial CuCo-BTC MOF shells through entropy-driven supramolecular assembly, and the morphology structure as illustrated in Figs. 10(b)–10(e). (3) Post-synthetic Ru^{3+} ion-exchange preceded gradient thermal processing: primary carbonization (700 °C, N_2, 2 h) induced metal nitride formation (CuCoN), followed by oxidative activation (300 °C, O_2/N_2=1:4) to engineer Ru/RuO_2 heterojunctions. The molecular sieving effect of MOF shell imposed ionic diffusion constraints, effectively inhibiting Oswald ripening and ensuring monodisperse shell architectures.

The template method is a commonly employed technique for preparing hollow structural functional materials, yet its significant drawbacks limit widespread application. Hard-template methods demand stringent conditions for template removal, such as employing strong acids or alkalis for silica and polystyrene templates. Moreover, hard-template structures exhibit limited

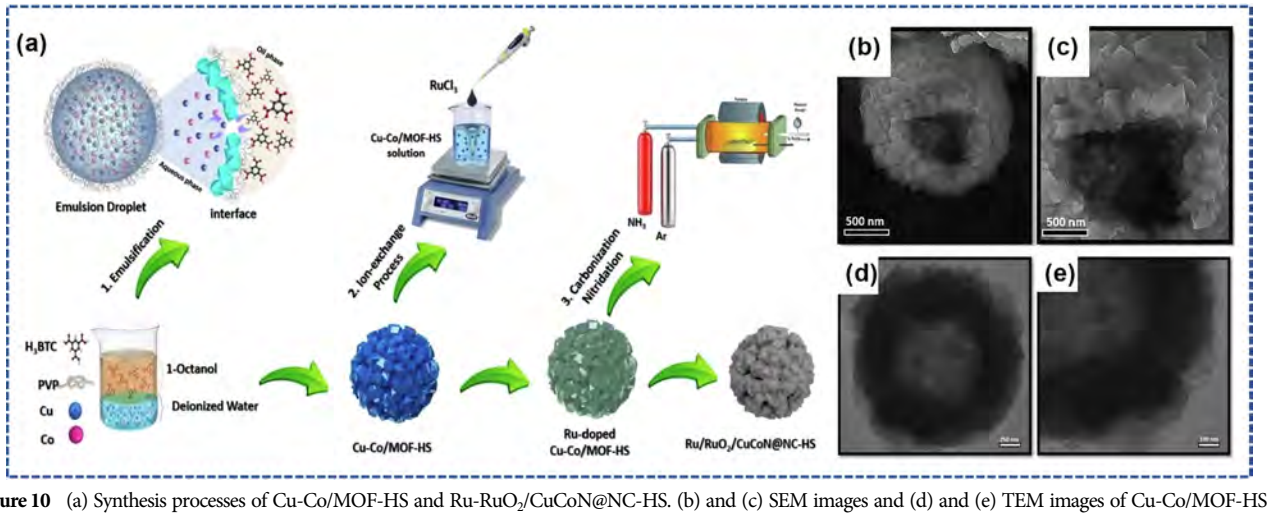

Figure 10 (a) Synthesis processes of Cu-Co/MOF-HS and Ru-RuO_2/CuCoN@NC-HS. (b) and (c) SEM images and (d) and (e) TEM images of Cu-Co/MOF-HS at different magnifications. (a–e) Reproduced with permission from Ref. [84], © 2022 Elsevier Inc.

diversity, yielding hollow structures with minimal morphological variation. Soft templates, whilst offering greater morphological flexibility and simpler removal, suffer from poor structural stability and low synthesis efficiency. Consequently, there is a pressing need to broaden the range of materials suitable for use as templates.

2.5 Self-catalytic pyrolysis method

Hollow nanoporous carbon structures (HNCs) hold significant application potential, yet their straightforward and efficient synthesis remains a challenge. The aforementioned strategies for synthesizing hollow-structured materials all involve multi-step reaction processes characterized by inherent complexity, requiring meticulous control over multiple interdependent variables.

Recently, Zhou et al. addressed this by modulating crystal growth kinetics to synthesize MOF precursors with heterogeneous crystallinity and diverse morphologies, which were directly converted into HNCs through a single-step pyrolysis process [85], and the synthesis process is shown in Fig. 11(a). This work represents the first demonstration of facile and versatile synthesis of functional HNCs from single-component MOF crystals. The protocol involved the following steps: Zn-MOF particles (denoted as STU-1) were synthesized by dissolving $Zn(NO_3)_2$ and 1,2-bis(5-imidazol-4-yl)methylene hydrazine in N, N-dimethylformamide (DMF). By tuning crystal growth parameters-including ligand/metal ion ratios, solvent composition, and temperature-STU-1 particles with varying morphologies were obtained, as illustrated in Figs. 11(b), 11(f), 11(h) and 11(j). A visual diagnostic method was developed to evaluate intracrystalline uniformity. Treatment with 6 M acetic acid selectively etched the core of crystallographically heterogeneous MOFs while leaving the outer shell intact (as evidenced in Fig. 11(c), whereas homogeneous crystals remained unaffected. For example, STU-1a (synthesized via solvothermal methods) yielded solid carbon spheres after pyrolysis. Acid etching confirmed its crystallographic homogeneity, as no core dissolution occurred. STU-1 particles with engineered crystallinity gradients, produced by adjusting growth kinetics in solution-phase reactions, underwent spontaneous cavity formation during pyrolysis. This process generated diverse HNC architectures, including yolk-shell polyhedrons, mesoporous frameworks, hollow microspheres, and hierarchical superstructures, as depicted in Figs. 11(d), 11(e), 11(g), 11(i) and 11(k). Mechanistic studies revealed that the self-driven hollowing arises from differential thermal contraction between the heterogeneous core and shell components of the MOF precursors during carbonization. This work establishes a generalizable strategy for tailoring HNC morphologies by leveraging crystallinity gradients in MOF templates.

3 Application of MOF-derived hollow materials for electrocatalysis

Water splitting and energy conversion technologies, including

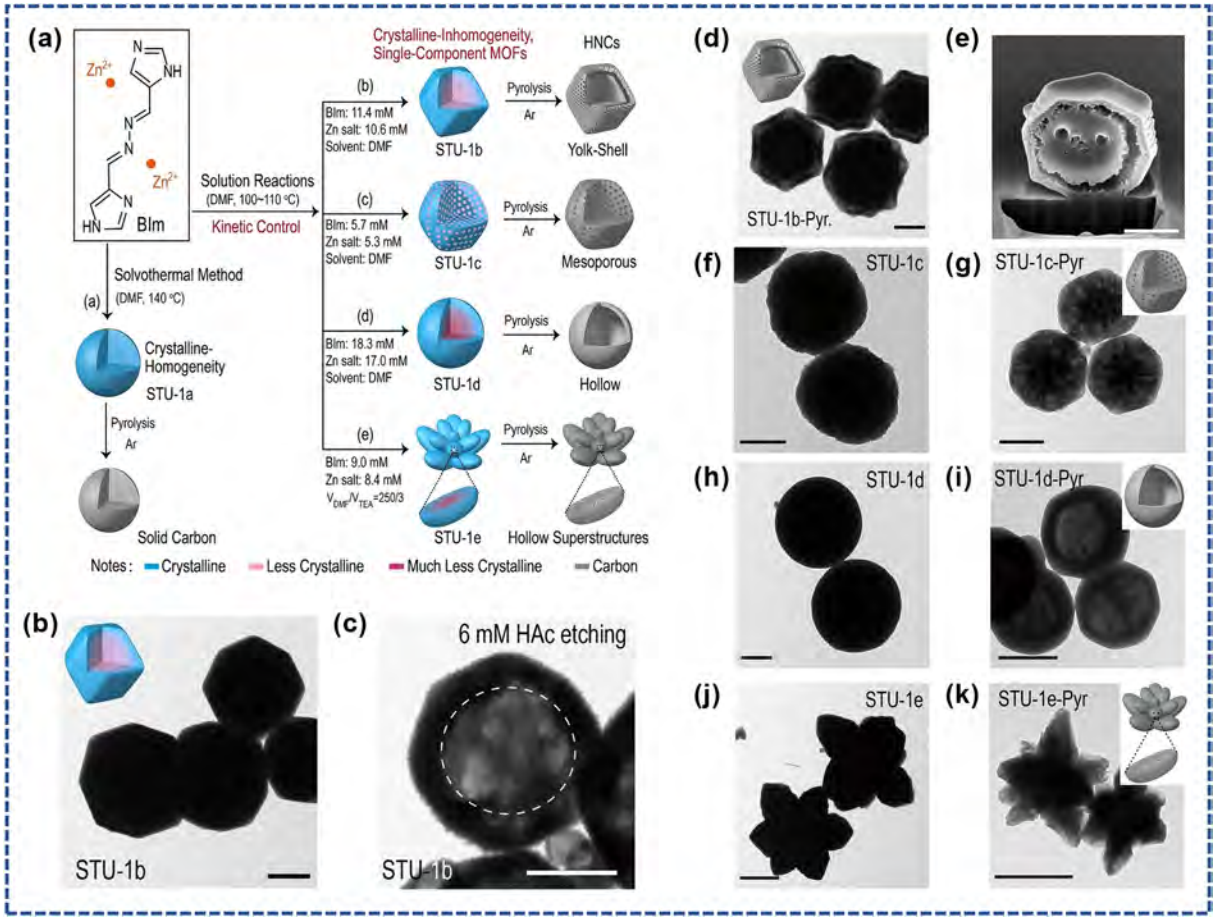

Figure 11 (a) Schematic illustration of the facile synthesis of HNCs (hollow nanocarbons) via crystalline uneven MOFs. (b, f, h, j) TEM images of as-synthesized STU-1b, STU-1c, STU-1d, and STU-1e solid microparticles. (d, g, i, k) TEM images of STU-1b, STU-1c, STU-1d, and STU-1e microparticles after pyrolysis. (c) TEM image of STU-1b microparticles after selective etching of a small amount of crystalline nucleus by dilute CH_3COOH aqueous solution (6 mM). (e) SEM image of the focused ion beam (FIB)-section after the pyrolysis of STU-1b at 900 °C. Scale bars: 1 μm. (a–k) Reproduced with permission from Ref. [85], © 2024 Wiley-VCH GmbH.

metal-air batteries and fuel cells, are crucial for addressing future resource and environmental challenges. The HER and OER are two critical half-reactions involved in the water-splitting process. Additionally, the OER and the ORR are of great importance in metal-air batteries. The four-electron ORR is also one of the most fundamental electrochemical reactions in fuel cells. The nanostructures of electrocatalytic materials can significantly alter their physical and chemical properties, making the rational design of the structures and compositions of MOF-derived materials beneficial to enhance their electrocatalytic performance [86, 87]. In recent years, significant efforts have been devoted to developing MOF-derived materials with superior HER, OER, ORR, and simultaneous bifunctional and trifunctional electrocatalytic activities. Hollow nanomaterials have gained increased attention due to their benefits in offering abundant active sites, a high electrode-electrolyte contact area, and enhanced charge transfer.

3.1 Hydrogen evolution reaction

The rapid depletion of fossil fuels is poised to trigger energy crises and exacerbate environmental problems. Hydrogen, as a clean energy source, is expected to replace traditional fossil fuels [88]. Hydrogen production driven from electrolyzed water is an efficient, environmentally friendly, and highly promising method to produce hydrogen. Pt and Pt-based catalysts are recently regarded as the most efficient HER catalysts due to their exceptional intrinsic activity and rapid reaction kinetics. However, their scarcity hinders large-scale commercial availability, prompting the development of non-precious metal materials with outstanding activity and stability [60, 89, 90]. Among the widely reported non-precious metal-based hollow electrocatalytic materials are metal oxides, alloys, transition metals, and their derivatives, such as metal nitrides, metal phosphides, and metal sulfides.

3.1.1 MOF-derived non-precious metal hollow electrocatalysts

Conductive metal-organic frameworks are effective electrocatalysts. Lou et al. successfully prepared Cu-MOF hollow structures supported on $Fe(OH)_x$ nanoboxes, specifically $Fe(OH)_x$@Cu-MOF NBs, through solvothermal reaction and selective redox etching using Cu_2O nanocubes as precursors (Figs. 12(a) and 12(b)) [91]. Characterization and theoretical analysis revealed that this unique structure features highly exposed ligand-unsaturated Cu_1-O_2 centers (Fig. 12(e)), which notably accelerate the efficient formation of the intermediate *H and enhance HER kinetics. The highly exposed active centers, enhanced charge transfer, and robust hollow nanostructures endow $Fe(OH)_x$@Cu-MOF NBs with excellent HER electrocatalysts. The prepared samples demonstrated an overpotential of 112 mV at a current density of 10 mA·cm^{-2} and a Tafel slope of 76 mV·dec^{-1}, as illustrated in Figs. 12(c) and 12(d). As previously demonstrated, Zhang et al. reported a one-step synthesis of CoRu@N-doped hollow nanostructured carbon (CoRu@NCHNS) materials using ZIF-67 as a precursor (Figs. 12(f) and 12(g)) [73]. This was accomplished through a simple liquid phase diffusion method and ion exchange strategy. The synergistic effect of CoRu alloy, the unique hollow structure, and N-doped contribute to the material exhibiting outstanding HER performance with an overpotential of 13 mV at a current density of 10 mA·cm^{-2} and a Tafel slope of 69.4 mV·dec^{-1}, as demonstrated in Figs. 12(h) and 12(i).

3.1.2 MOFs-derived transition metal-derived hollow electrocatalysts

Among transition metal elements, cobalt-based electrocatalysts, including their nitrides, phosphides, oxides, sulfides, and metallic cobalt, demonstrate exceptional HER properties, highlighting their promising potential for development. MOFs, especially cobalt-based zeolitic imidazolium frameworks (ZIF-67), serve as excellent precursors or templates for the preparation of non-noble metal electrocatalysts. Jeon et al. successfully prepared N-doped hollow nanocages composed of metallic cobalt/cobalt sulfide heterostructures (Co/Co_xS_y@NC-750) through a one-step pyrolysis method, assisted by H_2 reduction and sulfur powder sulfurization (Figs. 13(a) and 13(b)) [92]. The precise control of the pyrolysis temperature and its composition play a crucial role in materials engineering. The resulting materials exhibited remarkable HER activity with overpotentials and Tafel slopes of 130 mV (current density of 10 mA·cm^{-2}) and 82 mV·dec^{-1} in an acidic (0.5 M H_2SO_4) medium and 330 mV (current density of 10 mA·cm^{-2}) and 160 mV·dec^{-1} in basic (1.0 M KOH) medium, respectively, as shown in Figs. 13(c) and 13(d). In addition, the unique structure of the cobalt metal core/cobalt sulfide shell is conducive to maintaining long-term durability for over 30 h in

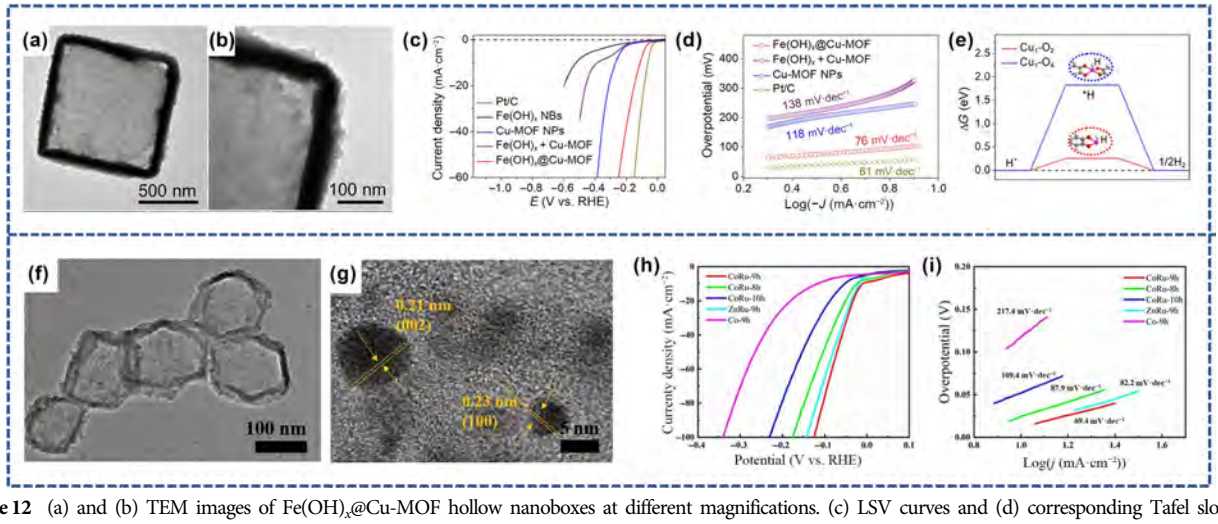

Figure 12 (a) and (b) TEM images of $Fe(OH)_x$@Cu-MOF hollow nanoboxes at different magnifications. (c) LSV curves and (d) corresponding Tafel slopes of $Fe(OH)_x$@Cu-MOF and other control materials. (e) Calculated free energy changes for *H adsorption on Cu sites of Cu_1-O_4 and Cu_1-O_2 centers. (a–e) Reproduced with permission from Ref. [91], © 2021 Cheng, W. R. et al. (f) and (g) TEM image of CoRu/PDA HNSs and HRTEM image of CoRu@NCHNSs; (h) LSV curves and (i) corresponding Tafel slopes of CoRu@NCHNSs. (f-i) Reproduced with permission from Ref. [73], © 2024 The Royal Society of Chemistry.

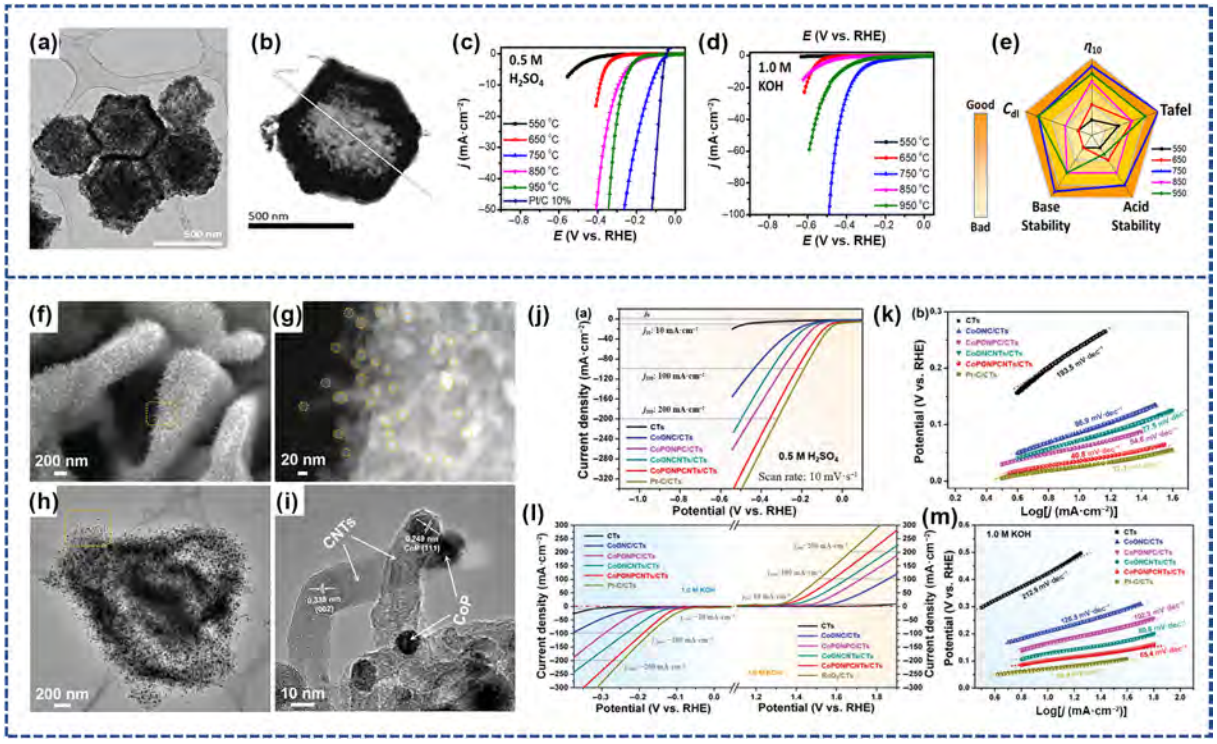

Figure 13 (a, b) TEM images of Co/Co_xS_y@NC. (c, d) LSV curves of Co/Co_xS_y@NC materials prepared at different temperatures in 0.5 M H_2SO_4 and 1.0 M KOH solutions. (e) Performance diagram comparing HER catalysts based on overpotential, Tafel plots, acid/alkali stability, and capacitance. (a–e) Reproduced with permission from Ref. [92], © 2024 The Royal Society of Chemistry. (f, g) SEM images, (h) TEM image, and (i) HRTEM image of CoP@NPCNTs. (j, k) LSV curves and corresponding Tafel slopes of CoP@NPCNTs in 0.5 M H_2SO_4, and (l, m) in 1.0 M KOH solutions. (f–m) Reproduced with permission from Ref. [93], © 2024 Wiley-VCH GmbH.

acid conditions and 40 h in alkaline conditions. Yang et al. reported the preparation of a novel braided hollow nanowall arrays with three-dimensional (3D) self-branched ultrasmall cobalt phosphide (CoP) nanoparticles embedded in N, P co-doped carbon nanotubes (CoP@NPCNTs) via a simple two-step pyrolysis synthesis strategy (Figs. 13(f)–13(i)) [93]. The Kirkendall effect induced the formation of irregular hollow nanowall arrays. The braided hollow nanowall arrays of N, P co-doped CNTs not only provide conductive support but also exhibit protective effects for the embedded CoP NPs. Meanwhile, the embedded CoP NPs provide abundant exposure active sites and short ion/electron diffusion pathways, enhancing the overall catalytic performance. The introduction of heteroatoms (N, P) can modulate the electronic structure of the catalyst surface, create more active defects and boost the catalytic activity. The material exhibited excellent HER performance in acidic and basic electrolytes. In acidic conditions (0.5 M H_2SO_4), it exhibited an overpotential of 53.1 mV at a current density of 10 mA·cm^{-2} and a Tafel slope of 40.8 mV·dec^{-1}, as illustrated in Figs. 13(j) and 13(k). In basic conditions (1.0 M KOH), the overpotential was 101.9 mV at the same current density and a Tafel slope of 65.4 mV·dec^{-1}, as depicted in Figs. 13(l) and 13(m). Moreover, theoretical calculations revealed that electron transfer occurred between the CNTs and the CoP NPs. Moreover, the CoP NPs not only enhanced the electronic states near the Fermi energy level of the Co d-orbitals but also increased the hydrogen bonding strength, resulting in improved electrocatalytic performance. Table 1 summarizes the applications of MOF-derived hollow functional materials synthesized in recent years in the electrocatalytic hydrogen evolution reaction, demonstrating their potential applications in water splitting.

3.2 Oxygen evolution reaction

As one of the half-reactions in water splitting, the OER involves a complex 4e$^-$ transfer process, and its slow kinetics greatly hinder the efficiency of hydrogen production via water splitting. Therefore, developing effective OER electrocatalysts to reduce the energy barrier of the OER reaction is crucial to improving the efficiency of overall water splitting. Currently, RuO_2 is the benchmark for OER electrocatalysts, but its high price and scarcity limit its large-scale application. Therefore, there is an urgent need to explore non-noble metal-based electrocatalysts with high activity, stability, and selectivity. MOF-derived catalysts with unique hollow structures involve more exposure to surface-active regions and high mechanical stability. Meanwhile, the structure and component tunability of MOFs enables them to exhibit synergistic physical or chemical properties, which has attracted considerable attention. Currently, more studied non-noble metal-based hollow electrocatalytic materials are metals/metal oxides and other metallizations (sulfides, nitrides, phosphides, etc.).

3.2.1 *Metals/metal oxides*

Qian et al. reported the synthesis of hollow structures from precursors via a simple ion exchange strategy (Figs. 14(a) and 14(b)) [94]. Then, the synthesis of hollow binary zeolite imidazolium salt frameworks and Prussian blue analog (PBA) heterostructures (ZIF-67@PBA) through a MOF-on-MOF hybrid approach uses ligand induction. After carbonization at 850 °C, the resulting material, Co_xFe-ZP, not only provided more active sites to improve the electrocatalytic OER performance but also encapsulated Co_xFe nanoparticles in carbon nanotubes to improve the material stability. The catalyst exhibited excellent OER performance with an overpotential of 302 mV at a current density

Table 1 Summary of the performance of MOF-derived hollow materials for HER

MOF-derived hollow structures	MOF Precursors	Performance	Reference electrode	Ref.
Ni-doped FeP/C hollow nanorods	MIF-88A nanorods	0.5 M H_2SO_4: $\eta_{10\ mA\cdot cm^{-2}}$ = 72 mV; Tafel slope = 54 mV·decade^{-1}; 1.0 M PBS (phosphate buffered saline): $\eta_{10\ mA\cdot cm^{-2}}$ = 117 mV; Tafel slope = 70 mV·decade^{-1}; 1.0 M KOH: $\eta_{10\ mA\cdot cm^{-2}}$ = 95 mV; Tafel slope = 72 mV·decade^{-1};	Ag/AgCl (KCl-saturated)	[56]
Hierarchical MoS_2/CoS_2 nanotube arrays	Co-MOF nanorod arrays	0.5 M H_2SO_4: $\eta_{10\ mA\cdot cm^{-2}}$ = 90 mV; Tafel slope = 30 mV·decade^{-1}; 1.0 M PBS: $\eta_{10\ mA\cdot cm^{-2}}$ = 150 mV; Tafel slope = 66.1 mV·decade^{-1}; 1.0 M KOH: $\eta_{10\ mA\cdot cm^{-2}}$ = 84 mV; Tafel slope = 34 mV·decade^{-1};	0.5 M H_2SO_4: saturated calomel electrode (SCE) 1.0 M PBS and 1.0 M KOH: Hg/HgO (1M KOH)	[66]
Hollow ZnS@Co_9S_8@Ni_3S_2 nanosword arrays	ZnCo MOFs nanosword arrays	1.0 M KOH: $\eta_{10\ mA\cdot cm^{-2}}$ = 97 mV; Tafel slope = 42.24 mV·decade^{-1};	Ag/AgCl (KCl-saturated)	[67]
N-doped carbon hollow nanostructure loaded with the CoRu alloy	ZIF-67 dodecahedron	1.0 M KOH: $\eta_{mA\cdot cm^{-2}}$ = 13 mV; Tafel slope = 69.4 mV·decade^{-1};	Hg/HgO	[73]
MOF-derived ultra-small Ru/RuO_2 nanoparticles doped in copper/cobalt nitride (CuCoN) encapsulated in nitrogen-doped nanoporous carbon framework	Bimetallic Cu-Co/MOF hollow nanospheres	1.0 M KOH: $\eta_{10\ mA\cdot cm^{-2}}$ = 41 mV; Tafel slope = 45 mV·decade^{-1};	Ag/AgCl (3 M KCl)	[84]
Hollow Fe(OH)$_x$@Cu-MOF nanoboxes	Cu_2O nanocube	1.0 M KOH: $\eta_{10\ mA\cdot cm^{-2}}$ = 112 mV; Tafel slope = 76 mV·decade^{-1}	Hg/HgO	[91]
Co/Co_xS_y nanoparticles within N-doped graphitic carbon	ZIF-67 dodecahedron	0.5 M H_2SO_4: $\eta_{10\ mA\cdot cm^{-2}}$ = 130 mV; Tafel slope = 82 mV·decade^{-1} 1.0 M KOH: $\eta_{10\ mA\cdot cm^{-2}}$ = 330 mV; Tafel slope = 160 mV·decade^{-1}	0.5 M H_2SO_4: SCE 1.0 M KOH: Hg/HgO	[92]
N, P-codoped carbon nanotubes knitted hollow nanowall arrays	Co-MOF carbon textiles	0.5 M H_2SO_4: $\eta_{mA\cdot cm^{-2}}$ = 53.1 mV; Tafel slope = 40.8 mV·decade^{-1} 1.0 M KOH: $\eta_{10\ mA\cdot cm^{-2}}$ = 101.9 mV; Tafel slope = 65.4 mV·decade^{-1}	SCE	[93]

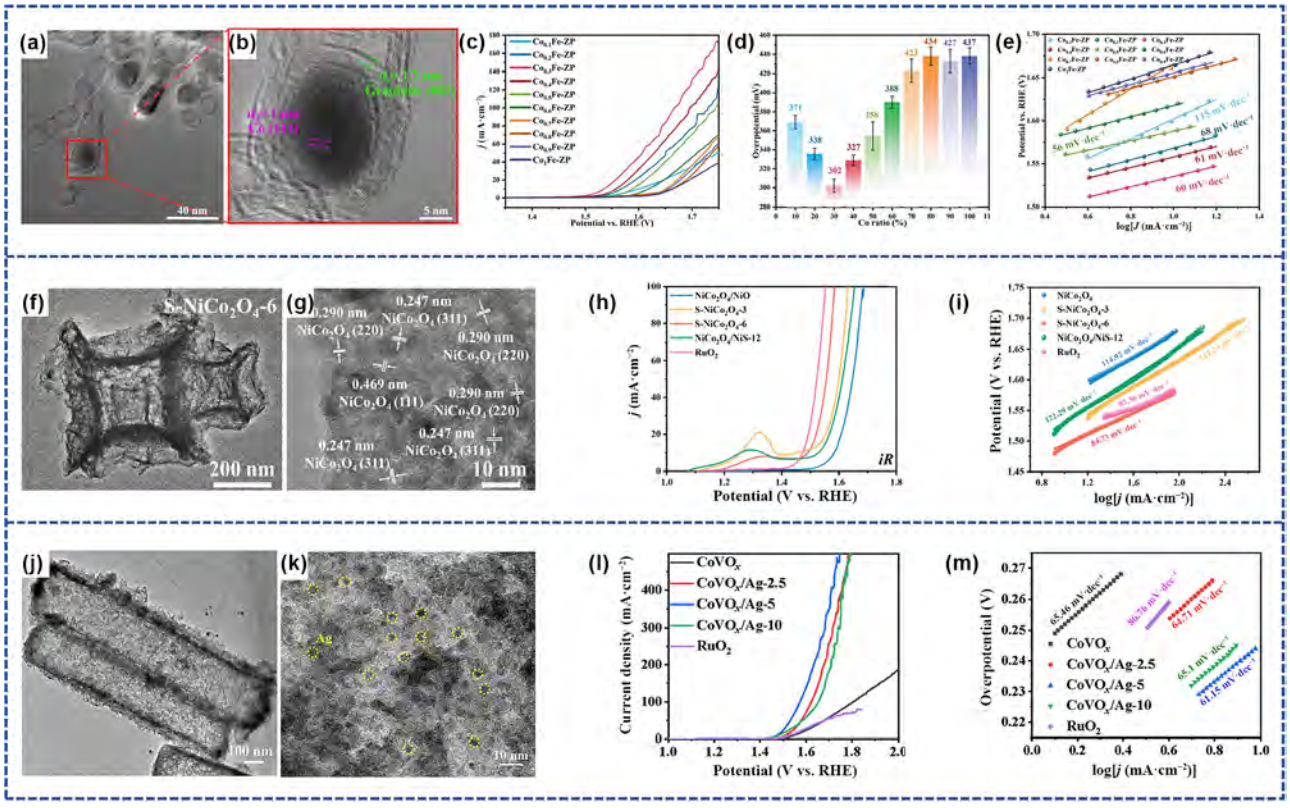

Figure 14 (a, b) HR-TEM images of Co_xFe-ZP. (c) LSV curve, (d) comparison of η_{10} values (representing the average of three repeated tests for the same sample), and (e) Tafel slope of Co_xFe-ZP in 1.0 M KOH solution. (a–e) Reproduced with permission from Ref. [94], © 2024 Elsevier Inc. (f) TEM image and (g) HR-TEM image of S-$NiCo_2O_4$ hollow cubic nanosheets. (h) *iR*-compensated LSV curve and (i) Tafel slope of the sample in 1.0 M KOH solution. (f–i) Reproduced with permission from Ref. [95], © 2023 Elsevier Inc. (j) and (k) TEM and HR-TEM images of $CoVO_x$/Ag. (l) LSV curve and (m) Tafel slope of $CoVO_x$/Ag in 1.0 M KOH solution. (j–m) Reproduced with permission from Ref. [96], © 2024 Elsevier Inc.

of 10 mA·cm^{-2} and a Tafel slope of 60.0 mV·dec^{-1} in 1.0 M KOH, as illustrated in Figs. 14(c)–14(e). The authors attributed the excellent OER performance as a result of the combination of morphology and composition through activation energy studies. Zhang et al. successfully synthesized sulfur-doped $NiCo_2O_4$ hollow cubic nanocages through a sophisticated ion-exchange methodology (Figs. 14(f) and 14(g)) [95]. The synthetic protocol commenced with the controlled growth of c-NiCo ZIF-67 nanocubes, where CTAB served as a facet-selective capping agent to regulate anisotropic crystal development. Subsequent introduction of sodium sulfide (Na_2S) initiated ligand-directed ion exchange, simultaneously inducing the liberation of undercoordinated Ni^{2+} and Co^{3+} cations. These metallic species subsequently underwent anion-mediated co-precipitation, yielding sulfur-doped NiCo-layered double hydroxide (S-NiCo-LDH) nanosheets preferentially aligned along the nanocube edges. Remarkably, this structural evolution occurred without compromising the parent ZIF-67's cubic framework. The observed bulk MOF/surface hydroxide coexistence stems from comparable ionic mobility between the constituent species: The minimal radius differential between Ni^{2+}/Co^{3+} and hydroxyl anions establishes a quasi-equilibrium in interdiffusion kinetics. Subsequent thermal treatment under aerobic conditions induced oxidative decomposition of organic linkers (liberated as CO_2), ultimately generating the distinctive hollow architecture. This study demonstrates that strategic sulfur doping coupled with optimized calcination parameters enables precise engineering of hollow nanostructures with preserved morphological fidelity and enhanced structural uniformity. Controlled S^{2-} coordination coupled with air annealing facilitates the formation of uniform hollow architectures, while simultaneous sulfur doping optimizes surface charge distribution, significantly enhancing oxygen evolution reaction (OER) activity. Under alkaline conditions (1.0 M KOH), the material exhibits an overpotential of 262 mV at 10 mA·cm^{-2} current density with a Tafel slope of 83.36 mV·dec^{-1}, as demonstrated in Figs. 14(h) and 14(i).

Li et al. synthesized $CoVO_x$/Ag with hollow nano-prismatic structure via a simple solvothermal and liquid phase stirring method using an ion-exchange strategy (Figs. 14(j) and 14(k)) [96]. The interaction of $CoVO_x$ and Ag nanoparticles optimized the electronic structure of the material, while the hollow structure provided more active sites, resulting in a significant enhancement of the OER performance. The overpotential is 247 mV at a current density of 10 mA·cm^{-2} and a Tafel slope of 61.15 mV·dec^{-1} under alkaline conditions (1.0 M KOH), as evidenced in Figs. 14(l) and 14(m). In addition, the material exhibited better stability, highlighting its potential to be used in hydrolysis.

3.2.2 *Other metallized materials*

Baeck et al. used an ion-exchange strategy and a two-step pyrolysis method to synthesize Fe and F double-doped hollow CoS_2 nanospheres (Fe-CoS_2-F) (Figs. 15(a) and 15(b)) [97]. The homogeneous hollow porous structure of Fe-CoS_2-F significantly increased the specific surface area and the number of exposed active sites. Moreover, the synergistic effect of Fe and F double doping optimized the electronic structure of the material, facilitating the adsorption/desorption of oxygen-containing reaction intermediates on the active sites during the OER process under alkaline conditions (1.0 M KOH). Theoretical calculations further demonstrated that the change of Gibbs free energy at the rate-determining step of the OER process (ΔG_{RDS}) was superior to that of the undoped material. Fe-CoS_2-F exhibits excellent OER activity, achieving an overpotential of 298 mV at a current density of 10 mA·cm^{-2} and a Tafel slope of 46.0 mV·dec^{-1}, as evidenced in Figs. 15(c) and 15(d). In a separate study, Lou et al. prepared trimetallic MOFs supported on S/N-doped macroporous carbon fibers by a cation exchange strategy (S/N-CMF@$Fe_xCo_yNi_{1-x-y}$-MOF) (Figs. 15(e) and 15(f)) [98]. Taking advantage of the inherent catalytic activity of the trimetallic and the increased active sites exposed on the hollow S/N-CMF matrix, S/N-CMF@$Fe_xCo_yNi_{1-x-y}$-MOF exhibits excellent basic OER activity and stability. The overpotential was 296 mV at a current density of 10 mA·cm^{-2} and a Tafel slope of 53.5 mV·dec^{-1} in 1.0 M KOH, as depicted in Figs. 15(g) and 15(h). The authors demonstrated through characterization and theoretical calculations that the formation of Fe/Co-doped γ-NiOOH after OER operation is responsible for its superior OER properties. Table 2 summarizes the applications of MOF-derived hollow functional materials

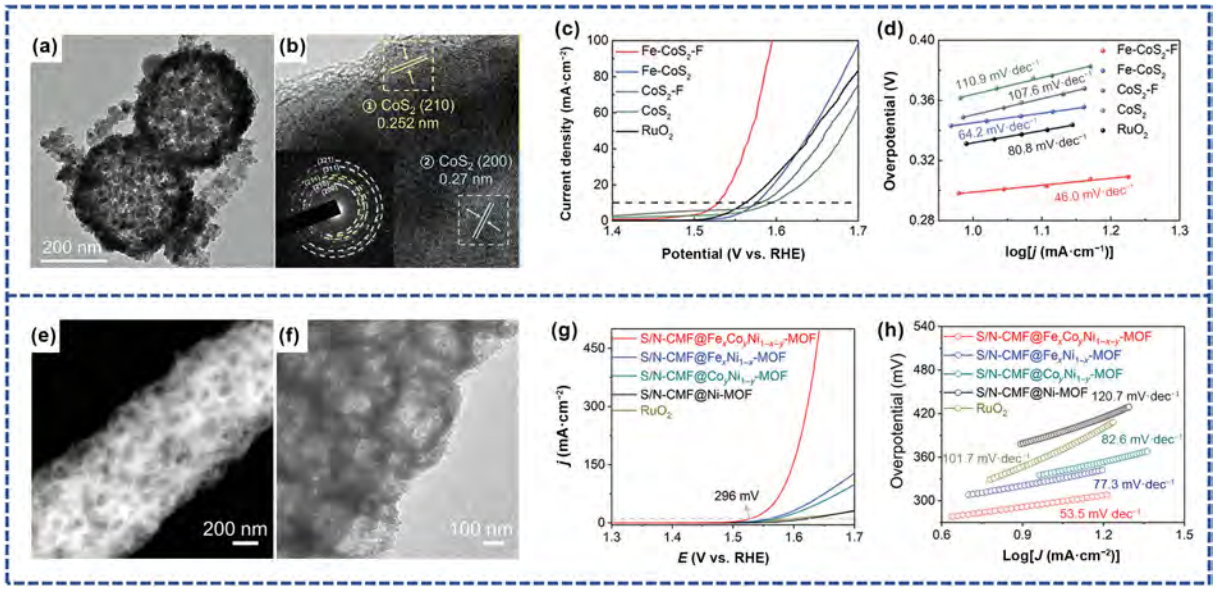

Figure 15 (a, b) TEM and HR-TEM images of Fe-CoS_2-F. (c) *iR*-compensated (85%) LSV curve and (d) Tafel slope of Fe-CoS_2-F in 1.0 M KOH solution. (a–d) Reproduced with permission from Ref. [97], © 2024 Elsevier Inc. (e, f) HAADF-STEM and TEM images of S/N-CMF@Ni-MOF. (g) LSV curve and (h) Tafel slope of S/N-CMF@Ni-MOF in 1.0 M KOH solution. (e–h) Reproduced with permission from Ref. [98], © 2023 Wiley-VCH GmbH.

Table 2 Summary of the performance of MOF-derived hollow materials for OER

MOF-derived hollow structures	MOF Precursors	Performance	Reference electrode	Ref.
Hollow ZnS@Co_9S_8@Ni_3S_2 nanosword arrays	ZnCo MOFs nanosword arrays	1.0 M KOH: $\eta_{20\ mA\cdot cm^{-2}}$ = 233 mV; Tafel slope = 100.69 mV·decade^{-1};	Ag/AgCl (KCl-saturated)	[67]
$(Ni,Fe)_2P$/C hollow nanorods	Ni-MOF nanorods	1.0 M KOH: $\eta_{10\ mA\cdot cm^{-2}}$ = 258 mV; Tafel slope = 45.5 mV·decade^{-1}	Ag/AgCl (saturated KCl solution)	[72]
N-doped carbon hollow nanostructure loaded with the CoRu alloy	ZIF-67 dodecahedron	1.0 M KOH: $\eta_{10\ mA\cdot cm^{-2}}$ = 238 mV; Tafel slope = 240.71 mV·decade^{-1};	Hg/HgO (1 M KOH)	[73]
Selenium-doped MOF CoS_2 hollow spheres	ZIF-67 hollow spheres	1.0 M KOH: $\eta_{10\ mA\cdot cm^{-2}}$ = 290 mV; Tafel slope = 50.8 mV·decade^{-1};	Ag/AgCl (saturated KCl solution)	[80]
MOF-derived ultra-small Ru/RuO_2 nanoparticles doped in copper/cobalt nitride (CuCoN) encapsulated in nitrogen-doped nanoporous carbon framework	Bimetallic Cu-Co/MOF hollow nanospheres	1.0 M KOH: $\eta_{10\ mA\cdot cm^{-2}}$ = 231 mV; Tafel slope = 81 mV·decade^{-1};	Ag/AgCl (3 M KCl)	[84]
Hollow MOF-on-MOF derived Fe-doped cobalt-carbon nanomaterials	Co_xZn_yZIF-67 dodecahedron	1.0 M KOH: $\eta_{10\ mA\cdot cm^{-2}}$ = 302 mV; Tafel slope = 60 mV·decade^{-1}	SCE	[94]
S-doped $NiCo_2O_4$ hollow cubic nanocage	NiCo ZIF-67 nanocubes	1.0 M KOH: $\eta_{10\ mA\cdot cm^{-2}}$ = 262 mV; Tafel slope = 83.36 mV·decade^{-1}	Ag/AgCl	[95]
Hollow $CoVO_x$/Ag	Co precursors	1.0 M KOH: $\eta_{10\ mA\cdot cm^{-2}}$ = 247 mV; Tafel slope = 61.15 mV·decade^{-1}	Ag/AgCl (KCl saturated)	[96]
Fe and F dual-doped CoS_2 hollow sphere	Co-glycerate nanosphere	1.0 M KOH: $\eta_{10\ mA\cdot cm^{-2}}$ = 298 mV; Tafel slope = 46.0 mV·decade^{-1}	Hg/HgO	[97]
$Fe_xCo_yNi_{1-x-y}$-MOF supported over S/N-doped carbon macroporous fibers	1D solid CdS@PAN fibers	1.0 M KOH: $\eta_{10\ mA\cdot cm^{-2}}$ = 296 mV; Tafel slope = 53.5 mV·decade^{-1}	Hg/HgO	[98]

synthesized in recent years in the electrocatalytic oxygen evolution reaction, demonstrating their potential applications in water splitting.

3.3 Oxygen reduction reaction

The ORR process involves multi-step adsorption of oxygen-containing intermediates, making the ORR activity of the electrocatalysts depend largely on the adsorption energy of oxygen-containing intermediates at catalysts' active sites. The adsorption energy is related to the electronic structure of the active site, which can be tuned through the structural and compositional design of the electrocatalyst.

3.3.1 MOFs-derived hollow materials for 4e⁻ ORR

Conducting hollow cobalt organic framework nanoboxes (Co-MOF NBs) (Figs. 16(a) and 16(b)) synthesized by Wang et al. using TA etching and a ligand exchange strategy as mentioned in the previous paper, which had excellent catalytic performance applied as electrocatalysts for 4e⁻ ORR. The resulting catalyst had a more positive half-wave potential of 0.88 V and a smaller Tafel slope of 35.4 mV·dec^{-1} in an alkaline solution, as illustrated in Figs. 16(c) and 16(d). Based on the cathode catalysts of Co-MOF NBs, the assembled zinc-air battery had an open circuit voltage of 1.46 V and a peak power density of 230 mW·cm^{-2}. Le et al. synthesized a heterogeneous zinc-air battery consisting of Fe_2NiO_4/$FeNiS_2$ nanosheet-assembled hollow microtubule (Fe_2NiO_4/$FeNiS_2$ MTs) structures through a sequential hydrothermal and calcination process (Figs. 16(e)–16(g)) [99]. The strong interactions between Fe_2NiO_4/$FeNiS_2$ nanosheets with Fe_2NiO_4 and $FeNiS_2$ at the heterogeneous interfaces tuned the electronic structure of the materials, leading to an increase in catalytic activity. The hollow structure effectively reduces the charge/mass transfer resistance and increases the surface area of the materials. The onset and half-wave potentials were 0.97 and 0.87 V, respectively, under alkaline conditions, and the assembled cathode material for zinc-air batteries exhibited outstanding cycling performance with a power density of 144.22 mW·cm^{-2} and more than 1500 cycles (40 min each) at a current density of 2.0 mA·cm^{-2}, as depicted in Figs. 16(h)–16(j). Peng et al. constructed a novel catalytic material with the construction of N-bridged Cu-Zn diatomic hollow carbon N-doped materials (Cu-Zn DA/HNC) via TA etching and the Kirkendall effect-pyrolysis strategy (Figs. 16(k) and 16(l)) [100]. The N atoms bridged between Cu and Zn atoms favor the enhancement of their synergistic effect, demonstrating a correspondingly enhanced O* binding capacity. Furthermore, the N-doped hollow structure favors mass transfer and exposure of more active sites. The resulting Cu-Zn DA/HNC exhibits excellent ORR activity in alkaline electrolytes (0.1 M KOH) with a half-wave potential of 0.82 V and a Tafel slope of 44 mV·dec^{-1}, as demonstrated in Figs. 16(m) and 16(n). As a cathode material applied to Zn-air electrodes, it has a long cycle life of up to 910 h and strong low-temperature (–40 °C) adaptability.

3.3.2 MOFs-derived hollow materials for 2e⁻ ORR

Currently, the industrial production of hydrogen peroxide (H_2O_2) relies on the anthraquinone method, which suffers from significant drawbacks such as large infrastructure requirements, complex operation, and high storage and transportation costs. In contrast, electrochemical synthesis has emerged as a promising alternative for direct on-site synthesis of H_2O_2 due to its safety, operational simplicity, and environmental friendliness. In recent years, the electrochemical two-electron oxygen reduction reaction (2e⁻ ORR) has attracted increasing attention as one of the most promising pathways for H_2O_2 production. However, this reaction competes with the four-electron ORR, which leads to the production of H_2O. Consequently, significant efforts have been devoted to the development of task-tailored electrocatalysts for selective O_2 to H_2O_2 reduction. MOF-derived hollow materials have been widely explored in electrocatalysis due to their unique structural features, but their application to the electrocatalytic production of H_2O_2 has been less studied. In recent years, porous

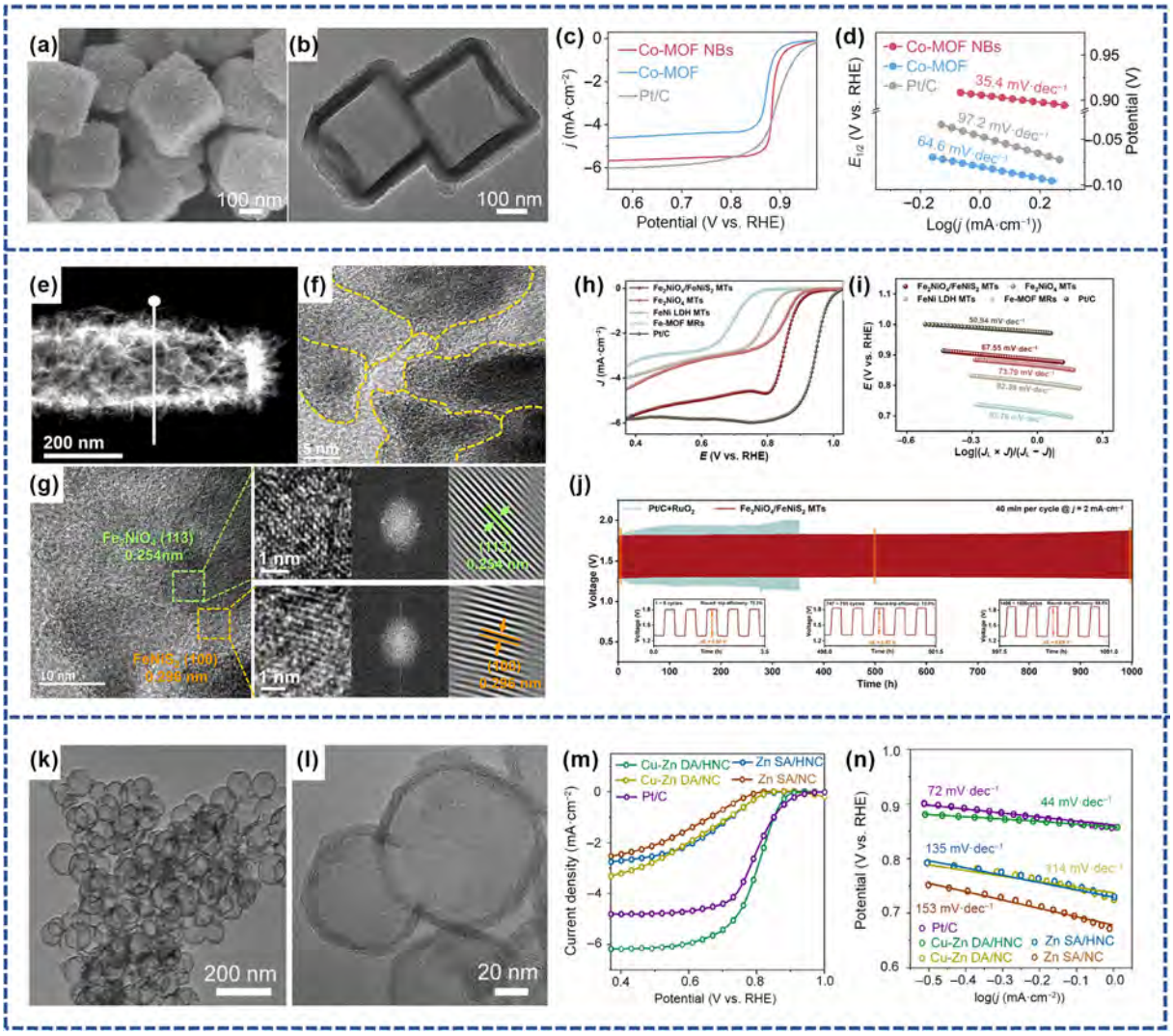

Figure 16 (a, b) SEM and TEM images of Co-MOF nanobelts (NBs). (c) LSV curve and (d) Tafel slope of Co-MOF NBs in 0.1 M KOH solution. (a–d) Reproduced with permission from Ref. [59], © 2024 Elsevier B.V. (e–g) TEM and HR-TEM images of $Fe_2NiO_4/FeNiS_2$ nanotubes (NTs). (h) LSV curve, (i) Tafel slope, and (j) cycling stability of $Fe_2NiO_4/FeNiS_2$ NTs during galvanostatic discharge/charge cycles at 2 mA·cm^{-2} in 0.1 M KOH solution (inset: cycling performance within 3.5 h per operation at initial, intermediate, and final cycles). (e–j) Reproduced with permission from Ref. [99], © 2024 Elsevier B.V. (k) and (l) TEM images of Cu-Zn dual-alloy/hollow nanocarbon (Cu-Zn DA/HNC). (m) LSV curve and (n) Tafel slope of Cu-Zn DA/HNC in 0.1 M KOH solution. (k–n) Reproduced with permission from Ref. [100], © 2024 Elsevier B.V.

conducting MOFs have been widely used in electrocatalysis due to their dispersed planar metal nodes and 2D π-conjugated structures. In addition, recent studies have shown that low-coordinated metal sites are beneficial in improving the catalytic performance and selectivity of catalysts. Lou et al. designed and synthesized a low-coordinated, 2D conducting Zn/Cu metal-organic framework supported on hollow nanocubes (Figs. 17(a) and 17(b)) [101]. The authors used zinc and copper molecular sieve imidazole framework (ZIF) nanocubic structures (ZnCu-ZIF NCs) as precursors, formed hollow nanocubic structures (PA-ZnCu HNCs) through etching with phytic acid (PA). Finally, they synthesized electrically conductive hollow MOFs by ligand replacement using 2,3,6,7,10,11-hexahydroxytriphenylene (HHTP). The prepared ZnCu-MOF (H) catalysts demonstrated excellent performance and selectivity in basic (0.1 M KOH) and neutral (0.1 M K_2SO_4) electrolytes, achieving exhibiting good 2e$^-$ ORR performance and selectivity up to exceeding 90% and Faraday efficiency of over 95% at a current density of 25.0 mA·cm^{-2}, as illustrated in Figs. 17(c)–17(f). Furthermore, ZnCu-MOF (H) also exhibits excellent stability over 80 h with negligible loss of Faraday efficiency and no structural degradation. Theoretical calculations indicate that ZnCu-MOF (H) with low coordination metal sites optimizes the adsorption/desorption capacity and energy barrier of the oxygen intermediates, as shown in Figs. 17(g) and 17(h). Table 3 summarizes the applications of MOF-derived hollow functional materials synthesized in recent years in oxygen reduction reactions, demonstrating their potential for use in fuel cells and on-site production of low-concentration hydrogen peroxide.

3.4 Others

3.4.1 *CO_2 reduction reaction*

CO_2 conversion and utilisation represent an effective measure for achieving carbon neutrality objectives, enabling the transformation of CO_2 into high-value-added products through electrochemical reactions [102]. CO_2 reduction reaction (CO_2RR) processes typically involve multiple electron and proton transfer

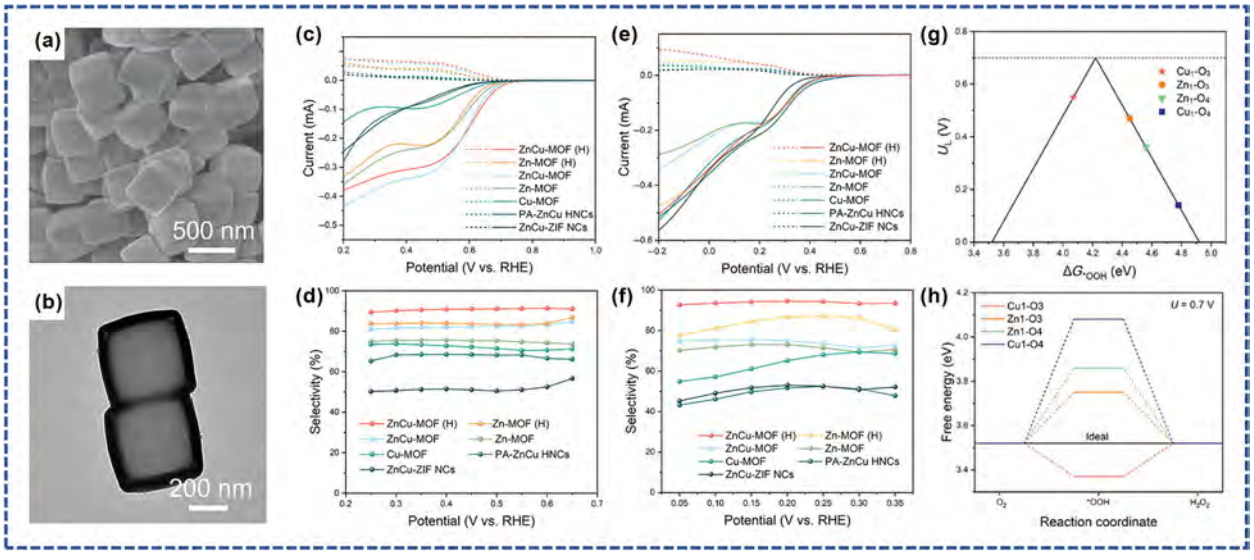

Figure 17 (a, b) SEM and TEM images of ZnCu-MOF(H). LSV curves and calculated selectivity of ZnCu-MOF(H) in (c, d) 0.1 M KOH solution and (e, f) 0.1 M K_2SO_4 solution. (g) Activity volcano plot and (h) free energy diagram for different sites (including Cu_1-O_3 and Zn_1-O_3 in ZnCu-MOF(H), and Zn_1-O_4 and Cu_1-O_4 in ZnCu-MOF) at $*U^*$ = 0.7 V. (a–h) Reproduced with permission from Ref. [101], © 2024 Pei, Z. H. et al.

Table 3 Summary of the performance of MOF-derived hollow materials for ORR

MOF-derived hollow structures	MOF Precursors	Performance	Reference electrode	Ref.
Hollow conductive Co-MOF nanoboxes	ZIF-67 nanocubes	0.1 M KOH: $E_{1/2}$ = 0.88 V vs. RHE; Tafel slope = 35.4 mV·decade^{-1}; n = 3.81	SCE	[59]
Nitrogen-Co-doped carbon composites with hollow-wall and 3D-ordered macroporous structures and hydrophilic surfaces	3D-ordered macroporous structures ZnCo-ZIF	0.1 M KOH: $E_{1/2}$ = 0.841 V vs. RHE; Tafel slope = 69 mV·decade^{-1}; n = 3.90	Ag/AgCl (saturated KCl solution)	[62]
Co/CoO heterojunction stitched in mulberry-like hollow N-doped carbon	MIF-88A nanorods	0.1 M KOH: $E_{1/2}$ = 0.83 V vs. RHE; Tafel slope = 96.8 mV·decade^{-1}	Ag/AgCl (saturated KCl solution)	[75]
Selenium-doped MOF CoS_2 hollow spheres	ZIF-67 hollow spheres	0.1 M KOH: E_{onset} = 0.952 V vs. RHE; $E_{1/2}$ = 0.88 V vs. RHE; Tafel slope = 49.8 mV·decade^{-1}	Ag/AgCl (saturated KCl solution)	[80]
Fe single-atom catalysts (s-Fe-HNC) with a hollow structure and ultrathin carbon shell	Fe-ZIF@PAA-SPB(spherical poly(acrylic acid) brush)	0.1 M KOH: $E_{1/2}$ = 0.83 V vs. RHE; Tafel slope = 42 mV·decade^{-1}; n = 3.90	Ag/AgCl (3 M KCl)	[83]
$Fe_2NiO_4/FeNiS_2$ hollow-structured microtubes	Fe-based MOFs microrods	0.1 M KOH: E_{onset} = 0.97 V vs. RHE; $E_{1/2}$ = 0.87 V vs. RHE; Tafel slope = 67.55 mV·decade^{-1}; n = 3.94	SCE	[99]
N-bridged Cu-Zn dual-atom supported on hollow N-doped carbon	Cu-Zn bimetallic MOF dodecahedron	0.1 M KOH: $E_{1/2}$ = 0.82 V vs. RHE; Tafel slope = 44 mV·decade^{-1}; n = 3.84–3.94	Ag/AgCl	[100]
2D conductive ZnCu MOFs hollow nanocubes	ZnCu-ZIF nanocubes	0.1 M K_2SO_4: H_2O_2 selectivity: over 90%; FE: 95% (25 mA·cm^{-2}); Tafel slope = 93 mV·decade^{-1}; n: close to 2 0.1 M KOH: E_{onset} = 0.74 V vs. RHE; H_2O_2 selectivity: over 90%; FE: 98% (25 mA·cm^{-2}); Tafel slope = 65 mV·decade^{-1} n: close to 2	Ag/AgCl (3 M KCl)	[101]

Note: The discrepancies in performance evaluation criteria primarily stem from variations in the data presented within the literature.

steps, yielding diverse C_1 to C_3 carbon-based products. Among these, CO stands as the core feedstock for basic chemical industries and holds the greatest economic value [103]. The CO_2 molecule possesses a highly symmetrical structure and a stable C=O bond. Consequently, achieving highly selective conversion from CO_2 to CO within a broad potential window while maintaining stability remains a key research focus. Chen et al. employed a melamine-assisted pyrolysis method to prepare self-supporting carbon hollow fibre electrodes (Ni-N_2-CHF) modified with an unsaturated Ni-N_2 coordination structure [104]. Through combined DFT calculations and experimental studies, the authors demonstrated that the unsaturated Ni-N_2 coordination structure reduces the energy barrier for forming the key reaction intermediate COOH* compared to the saturated Ni-N_4 structure, significantly enhancing the electrocatalytic activity for CO_2 reduction reactions. The Ni-N_2-CHF achieved over 90% CO Faraday efficiency and a partial current density of 61 mA·cm^{-2} in 0.5 M $KHCO_3$ solution, maintaining this high performance with excellent durability exceeding 100 hours. Gong et al. synthesised hollow carbon spheres (Ag@C) using SiO_2 spheres as templates through a series of processes: Ag nanoparticle loading, Stöber coating, high-temperature calcination, and chemical etching to remove the template [105]. These Ag@C structures exhibited highly efficient CO_2RR activity in strongly acidic electrolytes

(0.05 M H_2SO_4 and 0.5 M K_2SO_4, pH 1.1). Faraday efficiency exceeded 95% at a current density of 300 mA·cm^{-2}, with single-pass carbon efficiency (SPCE) reaching 46.2% at a CO_2 flow rate of 2 cm^3·min^{-1}. Stability was enhanced compared to alkaline conditions. Theoretical calculations revealed that the unique structure of Ag@C modulates OH^- and H^+ diffusion processes, confining the local reaction environment at high pH values to promote activity.

3.4.2 *N_2 reduction reaction*

Against the backdrop of the global energy crisis and environmental pollution, adjusting the production methods for industrial chemicals and energy represents an effective measure to alleviate this situation. As one of the world's most widely used inorganic chemicals, NH_3 is primarily employed in the production of inorganic fertilisers, explosives, nitric acid, and pharmaceutical intermediates [106]. The conventional Haber-Bosch process necessitates operation under elevated temperatures (350–550 °C) and pressures (150–350 Pa), consuming substantial electricity and generating significant CO_2 emissions [107, 108]. Electrochemical conversion of N_2 to NH_3 at ambient temperature and pressure represents a promising alternative approach. The primary challenge lies in activating inert nitrogen gas while suppressing the competing HER, necessitating the development of highly active, cost-effective electrocatalysts [109]. Huo et al. synthesised a hollow amorphous CrO_2/carbon hybrid amorphous metal catalyst ($HCrO_x$/C-550) featuring a multi-level porous structure through selective etching and controlled pyrolysis [110]. $HCrO_x$/C-550 exhibits outstanding electrocatalytic N_2 reduction reaction (N_2RR) performance at ambient temperature and pressure, demonstrating a yield of 19.10 μg·h^{-1}·mg$_{cat}^{-1}$ at –0.7 V vs. RHE in 0.1 M Na_2SO_4 electrolyte, with a Faradaic efficiency of 1.4%, alongside excellent structural and cycling stability. Notably, the amorphous metal oxide obtained via controlled pyrolysis possesses abundant unsaturated catalytic sites and optimised conductivity, attributable to the controllable metal-oxygen bond rearrangement and the doping effect of carbon materials from organic ligands.

4 Summary and outlook

The unique porosity and tunable chemical composition of morphological offering frameworks (MOFs) make them excellent precursors for constructing porous structures. Morphologically engineered hollow structures inherit the morphological features of their precursors while exhibiting highly exposed active sites and shorter charge and mass transfer paths. These advantageous properties accelerate the rate of charge transfer during electrocatalytic reactions, thereby enhancing the electrocatalytic performance. As a result, MOFs-based materials are particularly suitable as electrically charged electrodes in electrochemical applications. This review synthesizes recent advancements in the research of functional materials derived from MOFs as precursors for creating hollow structures, with a brief overview of their applications in electrocatalysis. Based on the characteristics of MOFs precursors, the commonly used synthesis strategies include acid etching strategies, ion exchange strategies, template-based methods, and self-catalytic thermal decomposition. Despite significant efforts dedicated to this field and notable progress achieved, challenges remain in the synthesis and application of hollow structure functional materials derived from MOFs precursors.

Firstly, the precise control of the structural and compositional complexity in hollow structures derived from multi-component MOFs precursors presents notable challenges. Although an increasing number of reports have been published on functional materials derived from MOFs hollow structures, there is a lack of universal theoretical guidance for the precise regulation of pore dimensions, shell thickness, and pore distribution. Additionally, in the context of acid etching strategies, the solubility and pH of the solvent play critical roles in determining the etching results. To achieve more generalized conditions, further investigation is required. Moreover, it is imperative to consider environmental impacts and explore greener synthesis pathways, such as the development of low-temperature solvent methods and the use of ionic liquids to minimize the reliance on organic reagents.

Secondly, the synergistic interactions among different components, including diverse atoms (e.g., N, S, P) and metal-based species (e.g., metal carbides, nitrides, phosphides), are crucial for enhancing electrocatalytic performance. In multi-component hybrid materials, each component contributes unique functionalities to address the limitations of individual components, thereby producing synergistic effects. However, conventional synthesis approaches for MOFs hollow materials predominantly utilize single-metal or dual/third-metal MOFs precursors. Future research should focus on the exploration of MOFs precursors containing multiple metal centers, aiming to exploit new opportunities arising from such materials.

Thirdly, the mechanistic understanding of the relationship between the structural features of MOFs hollow materials and their enhanced electrocatalytic performance remains incomplete. While structural and compositional correlations are often attributed to the synergistic effects of architecture and composition, a more detailed and accurate mechanistic explanation is still lacking. With advances in computer technology and theoretical computation, theoretical simulation calculations have provided an effective means for gaining deeper insights into catalytic reaction mechanisms and determining structure-activity relationships. However, the multifactorial nature of electrochemical processes means theoretical computational models alone are insufficient to fully elucidate the influence of heterogeneous interfaces and synergistic effects on catalytic reactions. In such circumstances, integrating theoretical calculations with advanced *in-situ* characterisation techniques, such as synchrotron X-ray diffraction (XRD), X-ray absorption spectroscopy (XAS), and *in-situ* TEM, will facilitate the investigation of relationships between structure and electrocatalytic performance.

Finally, the scaling up of MOFs hollow materials synthesis is of critical importance. Currently, many methods for constructing hollow structures are limited to laboratory-scale applications, with relatively low yields, rendering them unsuitable for industrial production. To meet the demands of industrial applications, it is essential to develop synthesis strategies that are compatible with industrial needs. Moreover, expanding the application scope of MOFs hollow materials from small-molecule conversions to large-molecule conversions is crucial to satisfy future energy demands.

In conclusion, the rapid development of MOFs-derived hollow structures has provided numerous new opportunities and challenges in the field of electrocatalysis. The pursuit of simpler and more customizable methods to synthesize desired structures and compositions for electrocatalytic materials and electrochemical materials will significantly advance energy conversion and storage technologies. We anticipate that, in the near future, MOFs-derived hollow materials will be better

equipped to meet practical application demands.

Acknowledgements

The authors express their appreciations for the financial support from the project of Zhongyuan Critical Metals Laboratory (GJJSGFYQ202422, GJJSGFYQ202315 and GJJSGFYQ202336). H. R. Xue acknowledges support from Zhongyuan Youth Talent Cultivation Project for Scientific and Technological Innovation.

Declaration of conflicting interests

The authors declare no conflicting interests regarding the content of this article.

Data availability

All data needed to support the conclusions in the paper are presented in the manuscript and/or the Supplementary Materials. Additional data related to this paper may be requested from the corresponding author upon request.

References

[1] Xue, Z. Q.; Liu, K.; Liu, Q. L.; Li, Y. L.; Li, M. R.; Su, C. Y.; Ogiwara, N.; Kobayashi, H.; Kitagawa, H.; Liu, M. et al. Missing-linker metal-organic frameworks for oxygen evolution reaction. *Nat. Commun.* **2019**, *10*, 5048.

[2] Beltrán, D. E.; Ding, S.; Xu, H.; Wu, G.; Litster, S. Air contamination of platinum-group metal-free fuel cell cathodes with atomically dispersed iron active sites. *Appl. Energy* **2023**, *349*, 121617.

[3] Chai, L. L.; Song, J. L.; Kumar, A.; Miao, R.; Sun, Y. Z.; Liu, X. G.; Yasin, G.; Li, X. F.; Pan, J. Q. Bimetallic-MOF derived carbon with single Pt anchored C_4 atomic group constructing super fuel cell with ultrahigh power density and self-change ability. *Adv. Mater.* **2024**, *36*, 2308989.

[4] Zaman, N.; Iqbal, N.; Noor, T.; Gao, J. K. Molten salt approach of zeolitic imidazole framework derived strontium doped porous carbon based bifunctional electrocatalysts for direct methanol fuel cell. *J. Power Sources* **2024**, *624*, 235541.

[5] Lee, K.; Lee, E.; Chang, H.; Roh, J.; Lee, S.; Bak, J.; Kwon, Y.; Ham, H. C.; Cho, E. Anchoring ordered PtZn nanoparticles on MOF-derived carbon support for efficient oxygen reduction reaction in proton exchange membrane fuel cells. *Chem. Eng. J.* **2025**, *505*, 159350.

[6] Yin, H. R.; Huang, M. H.; Wang, L. X.; Muhammad, S.; Isimjan, T. T.; Guo, J. Y.; Cai, D. D.; Wang, B.; Yang, X. L. Lattice-mismatched MOF-on-MOF nanosheets with rich oxygen vacancies show fast oxygen evolution kinetics for large-current water splitting. *Appl. Catal. B: Environ. Energy* **2025**, *367*, 125105.

[7] Xu, Y. Q.; Wang, R.; Feng, C.; Zhang, X.; Wang, N. N.; Zhang, Q.; Xie, M.; Xu, Y. C.; Jiao, Y.; Chen, J. R. Controlling the electronic structure of Fe-MOF electrocatalyst for enhanced water splitting and urea oxidation: A plasma-assisted approach. *J. Colloid Interface Sci.* **2023**, *650*, 1290–1300.

[8] Xu, H.; Shang, H. Y.; Wang, C.; Du, Y. K. Surface and interface engineering of noble-metal-free electrocatalysts for efficient overall water splitting. *Coord. Chem. Rev.* **2020**, *418*, 213374.

[9] Lv, J. Z.; Wang, Q. N.; OuYang, M. W.; Cao, Y. Highly performing sodium metal batteries reinforced by a self-regulated dual-layered solid electrolyte interphase via a metal-organic framework. *ACS Appl. Mater. Interfaces* **2024**, *16*, 41570–41582.

[10] Zhang, D. J.; Wang, W. J.; Li, S. M.; Shen, X. J.; Xu, H. Design strategies and energy storage mechanisms of MOF-based aqueous zinc ion battery cathode materials. *Energy Storage Mater.* **2024**, *69*, 103436.

[11] Gong, H.; Yue, M.; Xue, F.; Zhang, S. T.; Ma, M. T.; Mu, X. W.; Xue, H. R.; Ma, R. Z. Recent progress in advanced conjugated coordination polymers for rechargeable batteries. *Adv. Funct. Mater.* **2025**, *35*, 2411854.

[12] Song, M.; Zhang, Q.; Luo, G. Y.; Hu, H. Y.; Wang, D. L. Coordination structure engineering of single atoms derived from MOFs for electrocatalysis. *Coord. Chem. Rev.* **2025**, *523*, 216281.

[13] Xu, D. D.; Zhang, Z.; Tao, K.; Han, L. A heterostructure of a 2D bimetallic metal-organic framework assembled on an MXene for high-performance supercapacitors. *Dalton Trans.* **2023**, *52*, 2455–2462.

[14] Xu, Y. Y.; Xue, H. R.; Li, X. J.; Fan, X. L.; Li, P.; Zhang, T. F.; Chang, K.; Wang, T.; He, J. P. Application of metal-organic frameworks, covalent organic frameworks and their derivates for the metal-air batteries. *Nano Res. Energy* **2023**, *2*, e9120052.

[15] Su, Z. Y.; Huang, Q. P.; Guo, Q.; Hoseini, S. J.; Zheng, F. Q.; Chen, W. Metal-organic framework and carbon hybrid nanostructures: Fabrication strategies and electrocatalytic application for the water splitting and oxygen reduction reaction. *Nano Res. Energy* **2023**, *2*, e9120078.

[16] Deng, H. X.; Grunder, S.; Cordova, K. E.; Valente, C.; Furukawa, H.; Hmadeh, M.; Gándara, F.; Whalley, A. C.; Liu, Z.; Asahina, S. et al. Large-pore apertures in a series of metal-organic frameworks. *Science* **2012**, *336*, 1018–1023.

[17] Eddaoudi, M.; Sava, D. F.; Eubank, J. F.; Adil, K.; Guillerm, V. Zeolite-like metal-organic frameworks (ZMOFs): Design, synthesis, and properties. *Chem. Soc. Rev.* **2015**, *44*, 228–249.

[18] Cao, S.; Li, Y.; Tang, Y. J.; Sun, Y. Y.; Li, W. T.; Guo, X. T.; Yang, F. Y.; Zhang, G. X.; Zhou, H. J.; Liu, Z. et al. Space-confined metal ion strategy for carbon materials derived from cobalt benzimidazole frameworks with high desalination performance in simulated seawater. *Adv. Mater.* **2023**, *35*, 2301011.

[19] Ryu, U.; Jee, S.; Rao, P. C.; Shin, J.; Ko, C.; Yoon, M.; Park, K. S.; Choi, K. M. Recent advances in process engineering and upcoming applications of metal-organic frameworks. *Coord. Chem. Rev.* **2021**, *426*, 213544.

[20] Zhao, J. D.; Ren, G. M.; Meng, X. C. Recent advances on MOFs for photocatalytic and electrocatalytic nitrogen reduction to produce ammonia. *Nano Energy* **2024**, *130*, 110109.

[21] Mamaghani, A. H.; Liu, J. W.; Zhang, Z.; Gao, R.; Wu, Y. X.; Li, H. B.; Feng, M.; Chen, Z. W. Promises of MOF-based and MOF-derived materials for electrocatalytic CO_2 reduction. *Adv. Energy Mater.* **2024**, *14*, 2402278.

[22] Pan, H.; Zhao, G. C.; Hai, G. T.; Peng, B. X.; Gao, F. Y.; Zhang, C.; Wang, Y.; Huang, X. B. CeO_2-regulated NiCoOOH formed via electrocatalytic self-reconstruction of NiCoCe-MOFs for efficient electro-oxidation of 5-hydroxymethylfurfural. *J. Mater. Chem. A* **2024**, *12*, 29550–29561.

[23] Xu, M.; Wang, J. Y.; Liang, X.; Fang, W. Y.; Zhu, C. G.; Wang, F. W. MOF-derived ZrO_2–C nanoparticles modified PbO_2 electrode for high-efficiency electrocatalytic degradation of nitrophenolic compounds in wastewater. *Sep. Purif. Technol.* **2023**, *318*, 123921.

[24] Guo, W. H.; Pang, H. P.; Yang, X. Y.; Li, L.; Peng, J. X.; Zhao, M. Q.; Hou, C. C.; Zhu, Y. H.; Meng, F. L. Engineering modulated microscale assembly of MOF derived iron/nickel selenide for optimizing the oxygen evolution reaction. *J. Mater. Chem. A* **2024**, *12*, 15781–15791.

[25] Yang, Y. D.; Sun, Q. H.; Xue, J. H.; Xu, S. J.; Mao, L. J.; Miao, T. T.; Zhang, L. J.; Qian, J. J. MOF-derived N-doped carbon nanosticks coupled with Fe phthalocyanines for efficient oxygen reduction. *Chem. Eng. J.* **2023**, *464*, 142668.

[26] Lu, Z. J.; Wang, K.; Cao, Y. L.; Li, Y. Z.; Jia, D. Z. Amino-functionalized iron-based MOFs modified with 2D $FeCo(OH)_x$ hybrids for boosting oxygen evolution. *J. Alloys Compd.* **2021**, *871*, 159580.

[27] Xiong, L. L.; Zhang, Y. Y.; Wu, S. M.; Chen, F.; Lei, L. L.; Yu, L.; Li, C. M. Co_3O_4 nanoparticles uniformly dispersed in rational porous carbon nano-boxes for significantly enhanced

electrocatalytic detection of H_2O_2 released from living cells. *Int. J. Mol. Sci.* **2022**, *23*, 3799.
[28] Cheng, N. Y.; Liu, Q.; Asiri, A. M.; Xing, W.; Sun, X. P. A Fe-doped Ni_3S_2 particle film as a high-efficiency robust oxygen evolution electrode with very high current density. *J. Mater. Chem. A* **2015**, *3*, 23207–23212.
[29] Yang, W. X.; Wang, Z. C.; Zhang, W. Y.; Guo, S. J. Electronic-structure tuning of water-splitting nanocatalysts. *Trends Chem.* **2019**, *1*, 259–271.
[30] Liu, X. Y.; Lo, W. S.; Wu, C. H.; Williams, B. P.; Luo, L. S.; Li, Y.; Chou, L. Y.; Lee, Y.; Tsung, C. K. Tuning metal-organic framework nanocrystal shape through facet-dependent coordination. *Nano Lett.* **2020**, *20*, 1774–1780.
[31] Ma, M.; Ge, R. X.; Ji, X. Q.; Ren, X.; Liu, Z. A.; Asiri, A. M.; Sun, X. P. Benzoate anions-intercalated layered nickel hydroxide nanobelts array: An earth-abundant electrocatalyst with greatly enhanced oxygen evolution activity. *ACS Sustain. Chem. Eng.* **2017**, *5*, 9625–9629.
[32] Liu, Y. W.; Cheng, H.; Lyu, M. J.; Fan, S. J.; Liu, Q. H.; Zhang, W. S.; Zhi, Y. D.; Wang, C. M.; Xiao, C.; Wei, S. Q. et al. Low overpotential in vacancy-rich ultrathin $CoSe_2$ nanosheets for water oxidation. *J. Am. Chem. Soc.* **2014**, *136*, 15670–15675.
[33] Xu, H.; Song, P. P.; Fernandez, C.; Wang, J.; Zhu, M. S.; Shiraishi, Y.; Du, Y. K. Sophisticated construction of binary PdPb alloy nanocubes as robust electrocatalysts toward ethylene glycol and glycerol oxidation. *ACS Appl. Mater. Interfaces* **2018**, *10*, 12659–12665.
[34] Jin, L. J.; Xu, H.; Chen, C. Y.; Shang, H. Y.; Wang, Y.; Wang, C.; Du, Y. K. Three-dimensional PdCuM (M = Ru, Rh, Ir) trimetallic alloy nanosheets for enhancing methanol oxidation electrocatalysis. *ACS Appl. Mater. Interfaces* **2019**, *11*, 42123–42130.
[35] Salunkhe, R. R.; Kaneti, Y. V.; Kim, J.; Kim, J. H.; Yamauchi, Y. Nanoarchitectures for metal-organic framework-derived nanoporous carbons toward supercapacitor applications. *Acc. Chem. Res.* **2016**, *49*, 2796–2806.
[36] Tang, J.; Yamauchi, Y. MOF morphologies in control. *Nat. Chem.* **2016**, *8*, 638–639.
[37] Yan, L. T.; Cao, L.; Dai, P. C.; Gu, X.; Liu, D. D.; Li, L. J.; Wang, Y.; Zhao, X. B. Metal-organic frameworks derived nanotube of nickel-cobalt bimetal phosphides as highly efficient electrocatalysts for overall water splitting. *Adv. Funct. Mater.* **2017**, *27*, 1703455.
[38] Zheng, M. Y.; Du, J.; Hou, B. P.; Xu, C. L. Few-layered $Mo_{(1-x)}W_xS_2$ hollow nanospheres on Ni_3S_2 nanorod heterostructure as robust electrocatalysts for overall water splitting. *ACS Appl. Mater. Interfaces* **2017**, *9*, 26066–26076.
[39] Diao, X. M.; Zhang, X. W.; Li, Y.; Chen, X.; Zhao, Z. Y.; Wang, P.; Liu, P. P.; Gao, H. Y.; Wang, G. Heterogeneous network of 2D MOFs decorated 1D CNTs imparting multiple functionalities to composite phase change materials. *Nano Res. Energy* **2024**, *3*, e9120114.
[40] Huang, M. H.; Cao, C. S.; Liu, L.; Wei, W. B.; Zhu, Q. L.; Huang, Z. G. Controlled synthesis of MOF-derived hollow and yolk-shell nanocages for improved water oxidation and selective ethylene glycol reformation. *eScience* **2023**, *3*, 100118.
[41] Tian, J. J.; Cao, C. S.; He, Y. C.; Khan, M. I.; Wu, X. T.; Zhu, Q. L. Engineering hierarchical quaternary superstructure of an integrated MOF-derived electrode for boosting urea electrooxidation assisted water electrolysis. *Green Energy Environ.* **2024**, *9*, 695–701.
[42] Lou, X. W.; Archer, L. A.; Yang, Z. C. Hollow micro-/nanostructures: Synthesis and applications. *Adv. Mater.* **2008**, *20*, 3987–4019.
[43] Caruso, F.; Caruso, R. A.; Möhwald, H. M. Nanoengineering of inorganic and hybrid hollow spheres by colloidal templating. *Science* **1998**, *282*, 1111–1114.
[44] Chu, H. Q.; Zhang, D.; Jin, B. W.; Yang, M. Impact of morphology on the oxygen evolution reaction of 3D hollow cobalt-molybdenum nitride. *Appl. Catal. B: Environ* **2019**, *255*, 117744.
[45] Xia, W.; Mahmood, A.; Zou, R. Q.; Xu, Q. Metal-organic frameworks and their derived nanostructures for electrochemical energy storage and conversion. *Energy Environ. Sci.* **2015**, *8*, 1837–1866.
[46] Chen, Q. F.; Yao, M. Q.; Zhou, Y. Q.; Sun, Y. Y.; Zhang, G. X.; Pang, H. Etching MOF nanomaterials: Precise synthesis and electrochemical applications. *Coord. Chem. Rev.* **2024**, *517*, 216016.
[47] Li, Z.; Song, M.; Zhu, W. Y.; Zhuang, W. C.; Du, X. H.; Tian, L. MOF-derived hollow heterostructures for advanced electrocatalysis. *Coord. Chem. Rev.* **2021**, *439*, 213946.
[48] Cai, Z. X.; Wang, Z. L.; Kim, J.; Yamauchi, Y. Hollow functional materials derived from metal-organic frameworks: Synthetic strategies, conversion mechanisms, and electrochemical applications. *Adv. Mater.* **2019**, *31*, 1804903.
[49] Wang, H. F.; Chen, L. Y.; Pang, H.; Kaskel, S.; Xu, Q. MOF-derived electrocatalysts for oxygen reduction, oxygen evolution and hydrogen evolution reactions. *Chem. Soc. Rev.* **2020**, *49*, 1414–1448.
[50] Liang, Z. B.; Qiu, T. J.; Gao, S.; Zhong, R. Q.; Zou, R. Q. Multi-scale design of metal-organic framework-derived materials for energy electrocatalysis. *Adv. Energy Mater.* **2022**, *12*, 2003410.
[51] Zhang, Q.; Wang, W. S.; Goebl, J.; Yin, Y. D. Self-templated synthesis of hollow nanostructures. *Nano Today* **2009**, *4*, 494–507.
[52] Avci, C.; Ariñez-Soriano, J.; Carné-Sánchez, A.; Guillerm, V.; Carbonell, C.; Imaz, I.; Maspoch, D. Post-synthetic anisotropic wet-chemical etching of colloidal sodalite ZIF crystals. *Angew. Chem., Int. Ed.* **2015**, *54*, 14417–14421.
[53] Howarth, A. J.; Liu, Y. Y.; Li, P.; Li, Z. Y.; Wang, T. C.; Hupp, J. T.; Farha, O. K. Chemical, thermal and mechanical stabilities of metal-organic frameworks. *Nat. Rev. Mater.* **2016**, *1*, 15018.
[54] Xue, H. R.; Zhang, Z. H.; Lai, Y.; Gong, H.; Zhang, S. T.; Xia, W.; Li, J. J.; He, J. P. Construction of Co_2P nanoparticles anchored on hollow N-doped porous carbon nanoleaf for high-efficiency water splitting. *Chem. Eng. J.* **2024**, *483*, 149057.
[55] Khan, M. A. N.; Klu, P. K.; Xiao, C. M.; Qi, J. W.; Noor, T.; Sheikh, Z.; Kalwar, K.; Li, J. S. Hollow CoP/carbon as an efficient catalyst for the peroxymonosulfate activation derived from phytic acid assisted metal-organic framework. *Chemosphere* **2024**, *355*, 141775.
[56] Lu, X. F.; Yu, L.; Lou, X. W. Highly crystalline Ni-doped FeP/carbon hollow nanorods as all-pH efficient and durable hydrogen evolving electrocatalysts. *Sci. Adv.* **2019**, *5*, eaav6009.
[57] Zhang, X. K.; Hu, X.; Lv, S. X.; Li, Y.; Ren, J. R.; Huang, Y. M. Hollow NH_2-MIL-101@TA derived electrocatalyst for enhanced oxygen reduction reaction and oxygen evolution reaction. *Int. J. Hydrogen Energy* **2021**, *46*, 38692–38700.
[58] Lu, Y. B.; Zhang, G. X.; Zhou, H. J.; Cao, S.; Zhang, Y.; Wang, S. L.; Pang, H. Enhanced active sites and stability in nano-MOFs for electrochemical energy storage through dual regulation by tannic acid. *Angew. Chem., Int. Ed.* **2023**, *62*, e202311075.
[59] Wang, Y. L.; Zheng, Y.; Zheng, H. Y.; Zhang, G. T.; Zhang, X. Y.; Guo, Q. Y.; Dou, J.; Duan, J. L.; Lv, Q. L.; Tang, Q. W. Conductive cobalt-organic framework nanoboxes for efficient electrochemical oxygen reduction. *Appl. Catal. B: Environ. Energy* **2024**, *358*, 124447.
[60] Feng, J. R.; Lv, F.; Zhang, W. Y.; Li, P. H.; Wang, K.; Yang, C.; Wang, B.; Yang, Y.; Zhou, J. H.; Lin, F. et al. Iridium-based multimetallic porous hollow nanocrystals for efficient overall-water-splitting catalysis. *Adv. Mater.* **2017**, *29*, 1703798.
[61] Zhang, H. B.; Zhou, W.; Dong, J. C.; Lu, X. F.; Lou, X. W. Intramolecular electronic coupling in porous iron cobalt (oxy)phosphide nanoboxes enhances the electrocatalytic activity for oxygen evolution. *Energy Environ. Sci.* **2019**, *12*, 3348–3355.
[62] Yao, W.; Hu, A. Q.; Ding, J. T.; Wang, N. S.; Qin, Z.; Yang, X. F.; Shen, K.; Chen, L. Y.; Li, Y. W. Hierarchically ordered macro-mesoporous electrocatalyst with hydrophilic surface for efficient oxygen reduction reaction. *Adv. Mater.* **2023**, *35*, 2301894.

[63] Jiang, Z.; Lu, W. J.; Li, Z. P.; Ho, K. H.; Li, X.; Jiao, X. L.; Chen, D. R. Synthesis of amorphous cobalt sulfide polyhedral nanocages for high performance supercapacitors. *J. Mater. Chem. A* **2014**, *2*, 8603–8606.

[64] Hu, H.; Han, L.; Yu, M. Z.; Wang, Z. Y.; Lou, X. W. Metal-organic-framework-engaged formation of Co nanoparticle-embedded carbon@Co_9S_8 double-shelled nanocages for efficient oxygen reduction. *Energy Environ. Sci.* **2016**, *9*, 107–111.

[65] Guan, C.; Liu, X. M.; Elshahawy, A. M.; Zhang, H.; Wu, H. J.; Pennycook, S. J.; Wang, J. Metal-organic framework derived hollow CoS_2 nanotube arrays: An efficient bifunctional electrocatalyst for overall water splitting. *Nanoscale Horiz.* **2017**, *2*, 342–348.

[66] Tang, B. S.; Yu, Z. G.; Zhang, Y. X.; Tang, C. H.; Seng, H. L.; Seh, Z. W.; Zhang, Y. W.; Pennycook, S. J.; Gong, H.; Yang, W. F. Metal-organic framework-derived hierarchical MoS_2/CoS_2 nanotube arrays as pH-universal electrocatalysts for efficient hydrogen evolution. *J. Mater. Chem. A* **2019**, *7*, 13339–13346.

[67] Du, X. Q.; Ding, Y. Y.; Zhang, X. S. MOF-derived Zn–Co–Ni sulfides with hollow nanosword arrays for high-efficiency overall water and urea electrolysis. *Green Energy Environ.* **2023**, *8*, 798–811.

[68] Feng, L. L.; Li, G. D.; Liu, Y. P.; Wu, Y. Y.; Chen, H.; Wang, Y.; Zou, Y. C.; Wang, D. J.; Zou, X. X. Carbon-armored Co_9S_8 nanoparticles as all-pH efficient and durable H_2-evolving electrocatalysts. *ACS Appl. Mater. Interfaces* **2015**, *7*, 980–988.

[69] Wang, S. J.; Niu, M.; Zheng, J.; Liu, J. H.; Gao, Z. H.; Wang, P.; Ning, X.; Wang, Z. L.; Yamauchi, Y.; Ramakrishna, S. et al. Hollow porous CoP-carbon nanocages for hydrogen evolution reactions. *ACS Appl. Nano Mater.* **2024**, *7*, 12821–12829.

[70] Huang, M. H.; Zhou, S. H.; Yang, C. J.; Dong, C. L.; He, Y. C.; Wei, W. B.; Li, X. F.; Zhu, Q. L.; Huang, Z. G. Selenic acid etching assisted atomic engineering for designing metal-semimetal dual single-atom catalysts for enhanced CO_2 electroreduction. *ACS Nano* **2024**, *18*, 33210–33219.

[71] Zhou, S. H.; Wei, W. B.; Cai, X.; Ma, D. D.; Wang, S. M.; Li, X. F.; Zhu, Q. L. Customizing highly asymmetrical coordination microenvironment into P-block metal single-atom sites to boost electrocatalytic CO_2 reduction. *Adv. Funct. Mater.* **2024**, *34*, 2311422.

[72] Ramesh, S. K.; Son, J.; Ganesan, V.; Kim, J. Carbon-incorporated Ni_2P–Fe_2P hollow nanorods as superior electrocatalysts for the oxygen evolution reaction. *Nanoscale* **2022**, *14*, 16262–16269.

[73] Hu, Y.; Wang, C. C.; Liu, Y.; Lin, H. Y.; Zhang, K. Hollow structural materials derived from a MOFs/polymer loaded CoRu alloy for significantly boosting electrochemical overall water splitting. *J. Mater. Chem. A* **2024**, *12*, 6438–6445.

[74] Xiang, S. Y.; Qian, H. J.; Chen, Y. X.; Zhang, K.; Shi, Y. H.; Liu, W. D.; Sun, H. Z.; Sun, H. C.; Yang, B. Chelation competition induced polymerization (CCIP): A binding energy based strategy for nonspherical polymer nanocontainers' fabrication. *Chem. Mater.* **2017**, *29*, 6536–6543.

[75] Zhang, F. P.; Chen, L.; Zhang, Y. L.; Peng, Y. Y.; Luo, X.; Xu, Y. S.; Shi, Y. L. Engineering Co/CoO heterojunctions stitched in mulberry-like open-carbon nanocages via a metal-organic frameworks *in-situ* sacrificial strategy for performance-enhanced zinc-air batteries. *Chem. Eng. J.* **2022**, *447*, 137490.

[76] Guan, C.; Liu, X. M.; Ren, W. N.; Li, X.; Cheng, C. W.; Wang, J. Rational design of metal-organic framework derived hollow $NiCo_2O_4$ arrays for flexible supercapacitor and electrocatalysis. *Adv. Energy Mater.* **2017**, *7*, 1602391.

[77] Gu, Z. X.; Wei, X. L.; Zhang, X. Q.; Duan, Z. Y.; Gu, Z. W.; Gong, Q. Y.; Luo, K. Bimetallic-MOF-derived amorphous zinc/cobalt-iron-based hollow nanowall arrays via ion exchange for highly efficient oxygen evolution. *Small* **2021**, *17*, 2104125.

[78] Carpenter, B. P.; Talosig, A. R.; Rose, B.; Di Palma, G.; Patterson, J. P. Understanding and controlling the nucleation and growth of metal-organic frameworks. *Chem. Soc. Rev.* **2023**, *52*, 6918–6937.

[79] Alemán, J. V.; Chadwick, A. V.; He, J.; Hess, M.; Horie, K.; Jones, R. G.; Kratochvíl, P.; Meisel, I.; Mita, I.; Moad, G. et al. Definitions of terms relating to the structure and processing of sols, gels, networks, and inorganic-organic hybrid materials (IUPAC recommendations 2007). *Pure Appl. Chem.* **2007**, *79*, 1801–1829.

[80] Muthurasu, A.; Sampath, P.; Ko, T. H.; Lohani, P. C.; Pathak, I.; Acharya, D.; Chhetri, K.; Kim, D. H.; Kim, H. Y. Partial selenium surface modulation of metal organic framework assisted cobalt sulfide hollow spheres for high performance bifunctional oxygen electrocatalysis and rechargeable zinc-air batteries. *Appl. Catal. B: Environ.* **2023**, *330*, 122523.

[81] Tang, Y. J.; Shi, Y. X.; Su, Y. C.; Cao, S.; Hu, J. L.; Zhou, H. J.; Sun, Y. Y.; Liu, Z.; Zhang, S. T.; Xue, H. G. et al. Enhanced capacitive deionization of hollow mesoporous carbon spheres/MOFs derived nanocomposites by interface-coating and space-encapsulating design. *Adv. Sci.* **2024**, *11*, 2403802.

[82] Zhang, S. L.; Guan, B. Y.; Lou, X. W. Co–Fe alloy/N-doped carbon hollow spheres derived from dual metal-organic frameworks for enhanced electrocatalytic oxygen reduction. *Small* **2019**, *15*, 1805324.

[83] Fu, Z. N.; Wang, L. Z.; Zhang, W. J.; Tang, X.; Xia, W. X.; Li, J. X.; Wang, K. W.; Zhou, L. H.; Guo, X. H.; Dai, S. Facile synthesis of single-atom electrocatalysts with tailored carbon architectures via a polyelectrolyte brush-templated-growth approach. *J. Mater. Chem. A* **2023**, *11*, 17533–17541.

[84] Rezaee, S.; Shahrokhian, S. Ruthenium/ruthenium oxide hybrid nanoparticles anchored on hollow spherical copper-cobalt nitride/nitrogen doped carbon nanostructures to promote alkaline water splitting: Boosting catalytic performance via synergy between morphology engineering, electron transfer tuning and electronic behavior modulation. *J. Colloid Interface Sci.* **2022**, *626*, 1070–1084.

[85] Zheng, Z. L.; Wu, M. M.; Zeng, X.; Zhu, X. W.; Luo, D.; Chen, X. L.; Chen, Y. F.; Yang, G. Z.; Bin, D. S.; Zhou, X. P. et al. Facile fabrication of hollow nanoporous carbon architectures by controlling MOF crystalline inhomogeneity for ultra-stable Na-ion storage. *Angew. Chem., Int. Ed.* **2024**, *63*, e202400012.

[86] Zhang, L. J.; Mi, T. Q.; Ziaee, M. A.; Liang, L. F.; Wang, R. H. Hollow POM@MOF hybrid-derived porous $Co_3O_4/CoMoO_4$ nanocages for enhanced electrocatalytic water oxidation. *J. Mater. Chem. A* **2018**, *6*, 1639–1647.

[87] Tian, L.; Zhai, X. H.; Wang, X.; Li, J.; Li, Z. Advances in manganese-based oxides for oxygen evolution reaction. *J. Mater. Chem. A* **2020**, *8*, 14400–14414.

[88] Zhang, G.; Feng, Y. S.; Lu, W. T.; He, D.; Wang, C. Y.; Li, Y. K.; Wang, X. Y.; Cao, F. F. Enhanced catalysis of electrochemical overall water splitting in alkaline media by Fe doping in Ni_3S_2 nanosheet arrays. *ACS Catal.* **2018**, *8*, 5431–5441.

[89] Zhao, X. J.; Pachfule, P.; Li, S.; Simke, J. R. J.; Schmidt, J.; Thomas, A. Bifunctional electrocatalysts for overall water splitting from an iron/nickel-based bimetallic metal-organic framework/dicyandiamide composite. *Angew. Chem., Int. Ed.* **2018**, *57*, 8921–8926.

[90] Petrykin, V.; Macounova, K.; Shlyakhtin, O. A.; Krtil, P. Tailoring the selectivity for electrocatalytic oxygen evolution on ruthenium oxides by zinc substitution. *Angew. Chem., Int. Ed.* **2010**, *49*, 4813–4815.

[91] Cheng, W. R.; Zhang, H. B.; Luan, D. Y.; Lou, X. W. Exposing unsaturated Cu_1–O_2 sites in nanoscale Cu-MOF for efficient electrocatalytic hydrogen evolution. *Sci. Adv.* **2021**, *7*, eabg2580.

[92] Mai, H. D.; Park, P. M.; Bae, G. N.; Jeong, S.; Seo, B.; Cho, M.; Park, S.; Cuong, N. D.; Cuong, T. V.; Tran, N. M. et al. Metallic cobalt/cobalt sulfide hetero-nanostructures embedded within N-doped graphitic carbon nanocages for the hydrogen evolution reaction. *J. Mater. Chem. A* **2024**, *12*, 4761–4769.

[93] Kong, D. Z.; Xu, Q. G.; Chu, N. N.; Wang, H.; Lim, Y. V.; Cheng, J. B.; Huang, S. Z.; Xu, T. T.; Li, X. J.; Wang, Y. et al. Rational construction of 3D self-supported MOF-derived cobalt phosphide-

based hollow nanowall arrays for efficient overall water splitting at large current density. *Small* **2024**, *20*, 2310012.
[94] Ni, H. J.; Xu, S. J.; Lin, R.; Ding, Y.; Qian, J. J. Ligand-induced hollow binary metal-organic framework derived Fe-doped cobalt-carbon nanomaterials for oxygen evolution. *J. Colloid Interface Sci.* **2024**, *671*, 100–109.
[95] Luo, J. B.; Wang, X. Z.; Wang, S. T.; Li, W. L.; Li, Y. P.; Wang, T. Y.; Xu, F. Q.; Liu, Y.; Zhou, Y.; Zhang, J. MOF-derived S-doped $NiCo_2O_4$ hollow cubic nanocage for highly efficient electrocatalytic oxygen evolution. *J. Colloid Interface Sci.* **2024**, *656*, 297–308.
[96] Chen, S. R.; Yao, Y. Y.; Xu, J. L.; Chen, J. Y.; Wang, Z.; Li, P. Y.; Li, Y. Q. Hollow $CoVO_x$/Ag nanoprism with tailored electronic structure for high efficiency oxygen evolution reaction. *J. Colloid Interface Sci.* **2024**, *660*, 106–113.
[97] Kim, H.; Min, K.; Song, G.; Kim, J.; Ham, H. C.; Baeck, S. H. Hollow-structured cobalt sulfide electrocatalyst for alkaline oxygen evolution reaction: Rational tuning of electronic structure using iron and fluorine dual-doping strategy. *J. Colloid Interface Sci.* **2024**, *665*, 922–933.
[98] Zhao, Y. F.; Lu, X. F.; Wu, Z. P.; Pei, Z. H.; Luan, D. Y.; Lou, X. W. Supporting trimetallic metal-organic frameworks on S/N-doped carbon macroporous fibers for highly efficient electrocatalytic oxygen evolution. *Adv. Mater.* **2023**, *35*, 2207888.
[99] Li, X.; Nguyen, D. C.; Dong, K. X.; Prabhakaran, S.; Tran, D. T.; Kim, D. H.; Kim, N. H.; Le, J. H. Fe_2NiO_4/$FeNiS_2$ heterostructure-assembled hollow microtubes with numerous intimate interfaces as advanced catalyst for Zn-air battery. *Chem. Eng. J.* **2024**, *489*, 151210.
[100] Wu, K. L.; Li, S.; Hu, C.; Wen, G. Q.; Zeng, X. Z.; Wang, M. Y.; Wang, J. Y.; Chu, M. Y.; Shang, H. S.; Ye, M. F. et al. Nitrogen-bridged Cu–Zn dual-atom cooperative interface sites for efficient oxygen reduction reaction in Zn-air battery. *Appl. Catal. B: Environ. Energy* **2024**, *357*, 124288.
[101] Pei, Z. H.; Li, Y. X.; Fan, G. L.; Guo, Y.; Luan, D. Y.; Gu, X. Y.; Lou, X. W. Low-coordinated conductive ZnCu metal-organic frameworks for highly selective H_2O_2 electrosynthesis. *Small* **2024**, *20*, 2403808.
[102] Zhang, C. M.; Lin, Z. Y.; Jiao, L.; Jiang, H. L. Metal-organic frameworks for electrocatalytic CO_2 reduction: From catalytic site design to microenvironment modulation. *Angew. Chem., Int. Ed.* **2024**, *63*, e202414506.
[103] Sun, N. N.; Shah, S. S. A.; Lin, Z. Y.; Zheng, Y. Z.; Jiao, L.; Jiang, H. L. MOF-based electrocatalysts: An overview from the perspective of structural design. *Chem. Rev.* **2025**, *125*, 2703–2792.
[104] Wang, X. T.; Wei, Y. H.; Song, Y. F.; Mao, J. N.; Liu, X. H.; Li, S. J.; Li, G. H.; Zhu, H. Y.; Xia, J. Y.; Luo, C. et al. Carbon hollow fiber penetration electrode with unsaturated Ni–N_2 coordination for enhanced CO_2 electroreduction. *Adv. Sci.* **2025**, *12*, e02947.
[105] Li, X. Z.; Zhang, P.; Zhang, L. L.; Zhang, G.; Gao, H.; Pang, Z. F.; Yu, J.; Pei, C. L.; Wang, T.; Gong, J. L. Confinement of an alkaline environment for electrocatalytic CO_2 reduction in acidic electrolytes. *Chem. Sci.* **2023**, *14*, 5602–5607.
[106] Service, R. F. New recipe produces ammonia from air, water, and sunlight. *Science* **2014**, *345*, 610.
[107] Cherkasov, N.; Ibhadon, A. O.; Fitzpatrick, P. A review of the existing and alternative methods for greener nitrogen fixation. *Chem. Eng. Process.: Process Intensif.* **2015**, *90*, 24–33.
[108] Hochman, G.; Goldman, A. S.; Felder, F. A.; Mayer, J. M.; Miller, A. J. M.; Holland, P. L.; Goldman, L. A.; Manocha, P.; Song, Z.; Aleti, S. Potential economic feasibility of direct electrochemical nitrogen reduction as a route to ammonia. *ACS Sustain. Chem. Eng.* **2020**, *8*, 8938–8948.
[109] Jiang, B.; Xue, H. R.; Wang, P.; Du, H. R.; Kang, Y. Q.; Zhao, J. J.; Wang, S. Y.; Zhou, W.; Bian, Z. F.; Li, H. X. et al. Noble-metal-metalloid alloy architectures: Mesoporous amorphous iridium-tellurium alloy for electrochemical N_2 reduction. *J. Am. Chem. Soc.* **2023**, *145*, 6079–6086.
[110] Pan, T.; Wang, L.; Shen, Y.; Zhang, X. L.; Luo, C. Y.; Li, H. F.; Wu, P.; Zhang, H.; Zhang, W. N.; Savilov, S. V. et al. Amorphous chromium oxide with hollow morphology for nitrogen electrochemical reduction under ambient conditions. *ACS Appl. Mater. Interfaces* **2022**, *14*, 14474–14481.

Qingqing Yang received her BS degree from the Shenyang University of Technology in 2023. She is currently pursuing a master's degree at Zhengzhou University. Her research interests include carbon materials, MOF-derived materials, and their applications in electrocatalysis and fuel cells.

Hao Wan is an assistant professor of the Zhongyuan Critical Metals Laboratory at Zhengzhou University. He received his BSs (2013) and PhD (2019) from Central South University. From September 2016 to September 2018, he studied as an exchange student at the National Institute for Materials Science (NIMS) in Japan. His recent research interests include the design and synthesis of advanced nanostructures for electrochemical energy storage and conversion.

Ying Zhang is an assistant professor of the Zhongyuan Critical Metals Laboratory, School of Chemical Engineering at Zhengzhou University. He received his B.E. (2009) and PhD (2019) from the Central South University (China). He studied as a visiting researcher from 2017 to 2019 at the University of California San Diego (United States). Currently, his research focuses on natural resource derived nanostructures for energy storage and environmental applications.

Hairong Xue received his B.S. (2009), M.S. (2012) and PhD degree (2016) at the College of Material Science and Technology, Nanjing University of Aeronautics and Astronautics (NUAA, China). He worked as a lecturer at College of Chemical Engineering, Zhejiang University of Technology (ZJUT, China) after graduation. During 2018–2022, he has worked at National Institute for Materials Science (NIMS, Japan) as a Postdoctoral Fellow. Since 2023, he has been a Professor at Zhongyuan Critical Metals Laboratory, Zhengzhou University. His research interest centers on developing functional materials for energy storage and conversion.